

A deep *XMM-Newton* serendipitous survey of a middle-latitude area

II. New deeper X-ray and optical observations[★]

G. Novara^{1,2}, N. La Palombara¹, R. P. Mignani³, E. Hatziminaoglou⁴, M. Schirmer^{5,6},
A. De Luca^{1,2,7}, and P. A. Caraveo^{1,2}

¹ INAF-IASF, Istituto di Astrofisica Spaziale e Fisica Cosmica “G. Occhialini”, via Bassini 15, 20133 Milano, Italy
e-mail: novara@iasf-milano.inaf.it

² Università di Pavia, Dipartimento di Fisica Teorica e Nucleare, via Ugo Bassi 6, 27100 Pavia, Italy

³ Mullard Space Science Laboratory, University College London, Holmbury St Mary, Dorking, RH56NT, Dorking, UK

⁴ European Southern Observatory, Karl Schwarzschild Str.2, 85748 Garching, Germany

⁵ Isaac Newton Group of Telescopes, Apartado de correos 321, 38700 Santa Cruz de La Palma Tenerife, Spain

⁶ Argelander-Institut für Astronomie, Auf dem Hügel 71, 53121 Bonn, Germany

⁷ IUSS – Istituto Universitario di Studi Superiori, Viale Lungo Ticino Sforza 56, 27100 Pavia, Italy

Received 16 July 2008 / Accepted 21 March 2009

ABSTRACT

Context. The radio-quiet neutron star 1E1207.4–5209 has been the target of several *XMM-Newton* observations, with a total exposure of ~350 ks. The source is located at intermediate galactic latitude ($b \sim 10^\circ$), i.e. in a sky region with an extremely interesting mix of both galactic and extra-galactic X-ray sources.

Aims. The aim of our work is to investigate the properties of both the intermediate-latitude galactic and extra-galactic X-ray source populations in the 1E1207.4–5209 field.

Methods. We performed a coherent analysis of the whole *XMM-Newton* observation data set to build a catalogue of serendipitous X-ray sources detected with high confidence and to derive information on the source flux, spectra, and time variability. In addition, we performed a complete multi-band (*UBVRI*) optical coverage of the field with the *Wide Field Imager (WFI)* of the ESO/MPG 2.2 m telescope (La Silla) to search for candidate optical counterparts to the X-ray sources, down to a *V*-band limiting magnitude of ~24.5.

Results. From the combined observation data set we detected a total of 144 serendipitous X-ray sources. We find evidence that the source $\log N - \log S$ distribution may be different from those computed either in the Galactic plane or at high galactic latitudes. Thanks to the refined X-ray positions and to the *WFI* observations, we found candidate optical counterparts for most of the X-ray sources in our compilation. For most of the brightest ones we proposed a likely classification based on both the X-ray spectra and the optical colours.

Conclusions. Our results indicate that at intermediate galactic latitude the X-ray source population is dominated by the extra-galactic component, but with a significant contribution from the galactic component in the soft energy band, below 2 keV.

Key words. galaxies: Seyfert – X-rays: general

1. Introduction

Since the launch of *XMM-Newton* in 1999, the radio-quiet neutron star 1E1207.4–5209 in the supernova remnant (SNR) PKS 1209–51 has been the target of several observations, for a total of ~450 ks scheduled time. Therefore, observations of this field make up one of the deepest pencil-beam X-ray surveys obtained at intermediate galactic latitude ($|b| \approx 10^\circ$). This gives the unique opportunity to sample, in the same survey, both the galactic and extra-galactic X-ray source population. Thanks to the wide energy range, high throughput, and good spectral resolution of the *European Photon Imaging Camera (EPIC)* (Turner et al. 2001), this data set allows us to investigate with high sensitivity both the distant population of quasi-stellar objects (QSOs), active galactic nuclei (AGNs), normal galaxies, and the galactic population of stars and X-ray binaries (XRBs).

The two longest *XMM-Newton* observations, performed in August 2002 and corresponding to a total of ~260 ks of net integration time, were used to study the pulsations and the absorption features of the neutron star 1E1207.4–5209 (Bignami et al. 2003; De Luca et al. 2004). As a by-product, we used the data of the two *Metal Oxide Semi-conductor (MOS)* cameras to investigate the population of the faint *serendipitous* sources detected in the field. This yielded the detection of 196 serendipitous X-ray sources (Novara et al. 2006, hereafter Paper I), which were characterised by a very interesting $\log N - \log S$ distribution. On the one hand, in the 0.5–2 keV energy range it shows an excess with respect to both the Galactic plane and the high-latitude distributions, which suggests a mixed population composed of both galactic and extra-galactic sources. On the other hand, in the 2–10 keV energy band the $\log N - \log S$ distribution is comparable to that derived at high galactic latitudes, thus suggesting that it is dominated by extra-galactic sources. The cross-match of the list of serendipitous X-ray sources with version 2.3 of the

[★] Based on observations collected at ESO, La Silla, under Programmes 073.D-0621(A) and 074.D-0613(A).

Guide Star Catalogue (GSC 2.3) (Lasker et al. 2008) provided a candidate optical counterpart for about half of them, down to limiting magnitudes $B_J \sim 22.5$ and $F \sim 20$. For the 24 brightest sources it was possible to obtain a spectral characterisation, and an optical identification was proposed for $\sim 80\%$ of them. Finally, the detailed spectral investigation of one of the brightest sources, characterised by a highly absorbed spectrum and an evident Fe emission line, and its optical identification with the galaxy ESO 217-G29, led to it being classified as a new Seyfert-2 galaxy.

These results prompted us to extend our analysis to the whole sample of the *XMM-Newton* observations of the 1E1207.4–5209 field. In addition to the observations published in Bignami et al. (2003) and De Luca et al. (2004), we thus considered also the first observation of the field, performed in December 2001 (Mereghetti et al. 2002), and the sequence of the seven observations, performed during a 40 day window between June and July 2005 (Woods et al. 2007). In this way we almost doubled the total integration time and significantly increased the count statistics. We used this enlarged data set to refine the study of the serendipitous X-ray source population. We also took advantage of the improvements of the *XMM-Newton* data processing pipeline, which now minimises the number of spurious detections and provides improved source position errors (Watson et al. 2009). Moreover, we performed dedicated follow-up optical observations with the *Wide Field Imager (WFI)* of the ESO/MPG 2.2 m telescope down to $V \simeq 24.5$, i.e. with a factor of 10 improvement in flux limit compared to the *GSC 2.3* used in Paper I.

The paper is organised as follows: the X-ray observations and data reduction are described in Sect. 2, while the serendipitous source catalogue and the analysis of its bright subsample are presented and discussed in Sects. 3 and 4, respectively. The optical observations and data analysis are described in Sect. 5 and the cross-correlations of the X-ray and optical catalogues is described in Sect. 6. The optical/X-ray classification of the brightest sources, as well as of the peculiar Seyfert-2 galaxy, are discussed in Sect. 7.

2. X-ray observations and data processing

2.1. Observations

1E1207.4–5209 was observed with *XMM-Newton* in ten different pointings from 2001 December 23 to 2005 July 31, for a net exposure time of ~ 346 ks. All the three *EPIC* focal plane cameras (Turner et al. 2001; Strüder et al. 2001) were active during these pointings: the two *MOS* cameras were operated in standard *Full Frame* mode, in order to cover the whole $30'$ field-of-view; the *pn* camera was operated in *Small Window* mode, where only the on-target CCD is read-out, in order to time-tag the individual photons and provide accurate arrival time information. Since we are interested in serendipitous X-ray sources only, in the following analyses we consider only data taken with the *MOS* cameras.

In Table 1 we report the *good time intervals (GTI)* of the two *MOS* cameras for each of the ten observations, i.e. the “effective” exposure times computed after the soft-proton rejection (see next subsection). In the seven 2005 observations the CCD number 6 of the *MOS1* camera was not active, since it was switched off in March 2005 due to a micrometeorite impact¹. For the second and the third observations of Table 1 both *MOS* cameras were used with the thin filter, while the medium filter was used for all the other observations.

¹ http://xmm.vilspa.esa.es/external/xmm_news/items/MOS1-CCD6/index.shtml

Table 1. Log of the *XMM-Newton* observations of the 1E1207.4–5209 field with the corresponding net good time interval (GTI) for the two *EPIC/MOS* cameras.

Observation ID	<i>XMM-Newton</i> revolution	Date (UT)	GTI (ks)	
			<i>MOS1</i>	<i>MOS2</i>
0113050501	374	2001-12-23T18:59:41	24.3	25.2
0155960301	486	2002-08-04T07:25:09	105.3	105.8
0155960501	487	2002-08-06T07:17:29	100.7	102.0
0304531501	1014	2005-06-22T12:10:05	15.1	15.1
0304531601	1020	2005-07-05T00:44:58	18.3	17.9
0304531701	1023	2005-07-10T06:43:47	7.1	9.3
0304531801	1023	2005-07-11T02:00:45	56.6	54.5
0304531901	1024	2005-07-12T11:08:22	3.5	3.2
0304532001	1026	2005-07-17T00:18:21	12.7	10.7
0304532101	1033	2005-07-31T14:03:09	2.5	2.1

2.2. Data processing

For each pointing we obtained two data sets (i.e. one for each *MOS* camera), which we processed independently through the standard *XMM-Newton Science Analysis Software (SAS)* v.7.1.0. In the first step, the *XMM-Newton SAS* tasks *emproc* was used to linearize the *MOS* event files. In the second step, event files were cleaned up for the effects of soft protons flares. We filtered out time intervals affected by high instrument background induced by flares of soft protons (with energies less than a few hundred keV) hitting the detector surface. In order to avoid contributions from genuine X-ray source variability, we selected only single and double events ($PATTERN \leq 4$) with energies greater than 10 keV and recorded in the peripheral CCDs ($CCD = 2-7$). Then, we set a count-rate threshold for good time intervals (GTI) at 0.22 cts s^{-1} . By selecting only events within GTIs we finally obtained two “clean” event lists for each *MOS* data set, whose “effective” exposure times are reported in Table 1.

2.3. Source detection

The *EPIC* images of the 1E1207.4–5209 field show the presence of several faint X-ray sources. Therefore, we used a source detection algorithm in order to produce a catalogue of the serendipitous X-ray sources in the field.

We decided to perform the source detection in three different energy bands: the two standard coarse soft/hard energy bands 0.5–2 keV and 2–10 keV, and the total energy band 0.3–8 keV. First of all, for each observation in Table 1 we used the cleaned event file to produce *MOS1* and *MOS2* images in the three selected energy bands together with the associated exposure maps, and hence accounted for variations in spatial quantum efficiency (*QE*), mirror vignetting and effective field of view.

Although it would be interesting to look for variability on short time scales, we did not run the source detection for each of the ten observations in Table 1. Indeed, with the exceptions of the 2002 observations and the fourth 2005 observation, all observations have too short an integration time to allow for a statistically significant time variability analysis. As seen from Table 1, we thus divided the full observation set in two time windows: the first spanning from 2001 December 23 to 2002 August 6 (three observations), the second spanning from 2005 June 22 to 2005 July 31 (seven observations). We then ran the source detection on each of these two observation subsets separately, in order to search for long term source variability (Sect. 4.2).

We merged the cleaned event files of the 2001/2002 and 2005 observation subsets separately to obtain, for each of them, three

co-added images in the three selected energy bands. Since different observations correspond to different pointings, which have different aspect solutions, we corrected, for each of the three energy bands, the coordinates measured on the single observation *MOS1* and *MOS2* exposure maps through a relative coordinate transformation. To this aim, for each of the two time windows we selected the image with the longest exposure time and we took it as a reference to register all *MOS1* and *MOS2* exposure maps. We used the *IRAF* task `wregister` to compute the coordinate transformation and apply the frame registration. In this way, for each energy band we merged the exposure maps of each observation and *MOS* camera, thus obtaining total exposure maps corresponding to the co-added images built from the merged event file. For each observation subset, we then used three co-added images, one for each defined energy band, and the corresponding total exposure maps as input to run the source detection. Finally, we applied the same procedure to combine all the ten observations Table 1, so as to maximize the *signal-to-noise* (*S/N*) ratio. Below, we give details about the procedure used to run the source detection, for each energy band, in each of the three final data sets: those corresponding to the 2001/2002 and the 2005 observations (Table 1) and that corresponding to the full observation set.

1. For each data set, and for each energy band, we run the *SAS* task `eboxdetect` in *local mode* to create a preliminary source list. Sources were identified by applying the standard *minimum detection likelihood* criterion, i.e. we validated only candidate sources with detection likelihood $-\ln P \geq 8.5$ (Novara et al. 2006), where P is the probability of a spurious detection due to a Poissonian random fluctuation of the background. This corresponds to a probability $P = 2 \times 10^{-4}$ that the source count number in a given energy band originates from a background fluctuation. This implies a contamination of at most 1 spurious source per energy band.
2. Then, the task `esplinemap` was run to remove all the validated sources from the original image and to create a background map by fitting the so called *cheesed image* with a cubic spline.
3. For each data set, and for each energy band, the task `eboxdetect` was run again in *map mode*, using as a reference the computed background map. For each set, the likelihood values from each individual energy band were then added and transformed to *equivalent single band* detection likelihoods, and a threshold value of 8.5 was applied to accept or reject a detected source.

Unfortunately, even using the maximum number of spline nodes (20), the fit performed in step 2 (see above) is not sufficiently flexible to model the local variations of the background, due to the presence of the bright SNR PKS 1209–51. Therefore, it was necessary to correct each background map *pixel by pixel*, measuring the counts both in the *cheesed image* and in the background map itself by applying the correction algorithm described in Baldi et al. (2002). All sources were then checked against the corrected background maps and all their parameters calculated again. Finally, for each energy band, the revised source list was filtered to include, again, only sources with corrected detection likelihood $-\ln P > 8.5$.

2.4. Source list

At the end of the source detection process we thus produced, for each of the three observation sets, a master list including only sources with detection likelihood $-\ln P > 8.5$ in *at least*

one of the three energy bands and manually screened to reject residual false detections. For each source, the master list provides various parameters including the detector and sky coordinates, the effective exposure time and, for each of the three energy bands (soft/hard/total), the total counts, count-rate and errors, the *S/N* ratio, and the detection likelihood. The master list does not include quantitative information on the source extension, which can be used for a preliminary morphological classification (point-like or extended). This is because the significant distortion of the PSF at large off-axis angles (where most serendipitous sources are detected), together with the coarse spatial resolution of the *MOS* cameras ($1'1/\text{pixel}$), would make the determination of the source extension uncertain. In order to estimate a sky coordinate uncertainty for all the detected sources, we recomputed their positions using the task `emldetect`, which performs maximum likelihood fits to the source spatial count distribution. In this case, we fixed the threshold values of the equivalent single band detection likelihood (parameter *mlmin*) to 30, in order to select only high-confidence sources.

Our master lists contain a total of 132 sources for the 2001/2002 observation subset, 107 sources for the 2005 subset, and 144 sources for the whole observation set. Although we performed the source detection using the same tasks, the master list presented in Paper I contained 196 sources for the 2002 observations only. The difference between the number of sources in the two lists is mainly due to the improvement of the task `eboxdetect` in the *SAS* v.7.1.0, which was used to perform the source detection. The task now allows for a more accurate analysis in regions of diffuse emission, thus reducing the detection of spurious sources. Moreover, we now applied tighter selection criteria in order to qualify an X-ray source as real.

We note that in the field of 1E1207.4–5209 the *Incremental Second XMM-Newton Serendipitous Source Catalogue*² (2*XMMi*, Watson et al. 2008; Watson et al. 2009) reports 344 sources against the 144 found by our source detection procedure. We attribute this discrepancy mainly to the difference in the threshold value of the *detection likelihood* used in our procedure and in the procedure used to produce the 2*XMMi* catalogue. In our case, the detection likelihood is set to 8.5 for the *likemin* parameter of the *SAS* task `eboxdetect` and to 30 for the *mlmin* parameter of the *SAS* task `emldetect`, while for the generation of the 2*XMMi* catalogue these parameters were set to 5 and 6, respectively³. In other words, we applied much tighter criteria to the source selection, thus rejecting several low-confidence or spurious sources which are, instead, included in the 2*XMMi* catalogue. This is proven by Fig. 1, where the sources detected by our procedure are compared with the 2*XMMi* ones. As is apparent, while all our sources have a 2*XMMi* counterpart, the vast majority of the additional 2*XMMi* sources are either very faint, or detected at the edge of the *field-of-view*, or in region of diffuse X-ray emission. Therefore, it is quite likely that a large fraction of these sources are actually spurious.

In order to perform a detailed statistical analysis we also computed, for all the observation sets, the number of sources detected in each of the three energy bands. We summarised these numbers in Table 2 where we also reported their relative fraction with respect to the total number of sources detected in at least one energy band. We note that almost all sources are detected in

² http://xmmssc-www.star.le.ac.uk/Catalogue/xcat_public_2XMMi.html

³ http://xmmssc-www.star.le.ac.uk/Catalogue/UserGuide_xmmcat.html

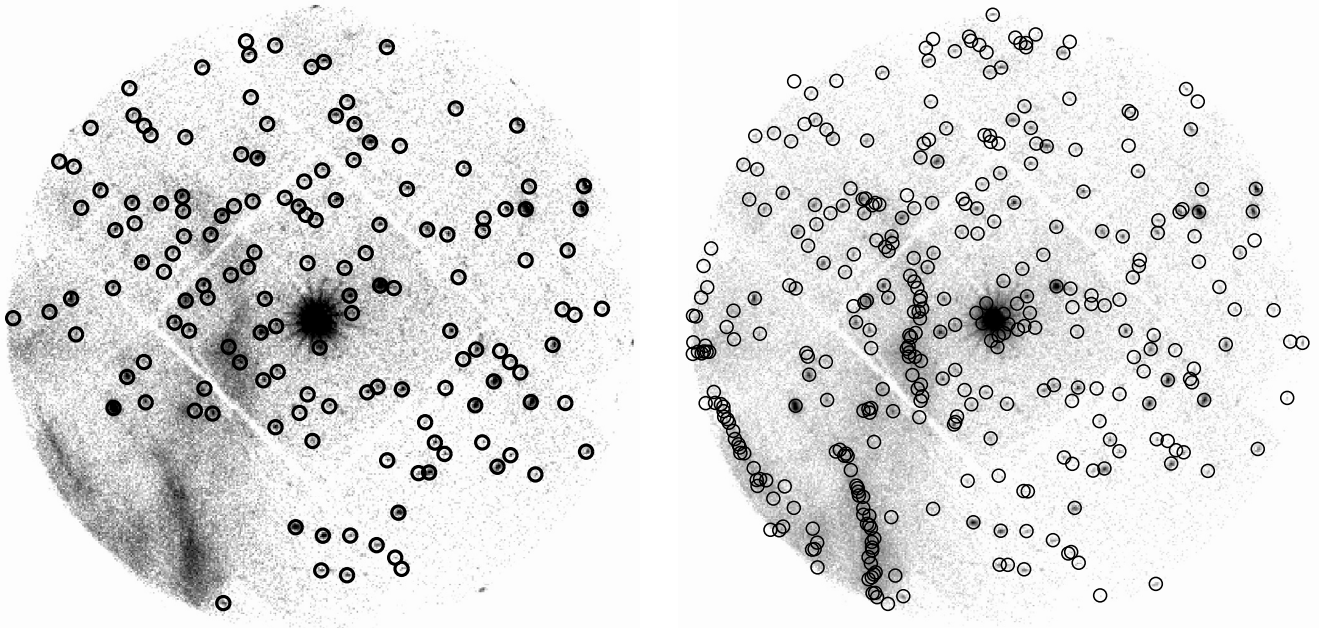


Fig. 1. *Left:* distribution of the 144 X-ray sources detected in the *EPIC/MOS* image of 1E1207.4–5209 in the energy range 0.3–8 keV. *Right:* distribution of the 344 X-ray sources listed in the *2XMMi* catalogue in the same sky region.

Table 2. Number of X-ray sources detected in each energy band and relative fraction for the three observation sets defined in Sect. 2.3.

Band (keV)	0.5–2	2–10	0.3–8	Total
Set	<i>N</i> (%)	<i>N</i> (%)	<i>N</i> (%)	<i>N</i>
1	101 (76.5)	68 (51.5)	123 (93)	132
2	84 (78.5)	42 (39)	97 (90.6)	107
3	114 (72)	87 (60)	135 (94)	144

the total energy band (0.3–8 keV), with a good fraction of them also detected in the soft energy band (0.5–2 keV). The number of sources detected in each energy band is different across the three observation sets, which is an effect of the uneven effective exposure times. This is evident in the case of the 2005 observation subset (see Table 1).

3. The serendipitous X-ray source catalogue

3.1. Catalogue description

We used the source master list obtained from the whole observation set to build a detailed catalogue of serendipitous X-ray sources detected in the 1E1207.4–5209 field. The complete serendipitous source catalogue is made available in electronic form through the *Vizier* database server. Each source was assigned a unique identifier using the recommended *XMM-Newton* designations for serendipitous sources. The catalogue information include most of the parameters already included in the master list, i.e. sky coordinates and associated uncertainty, effective exposure time, total counts, count-rate and errors, *S/N* ratio, and detection likelihood. In addition, we provided information on the source spectral parameters and the computed fluxes in the soft/hard/total energy bands.

Since for most sources the measured counts are too few to produce significant X-ray spectra, we used the *Hardness Ratio* (*HR*) to provide qualitative spectral information. The *HR* was computed from the measured count-rate (*CR*) in the hard

(2–10 keV) and soft (0.5–2 keV) energy bands and is defined according to the equation:

$$HR = \frac{CR(2-10) - CR(0.5-2)}{CR(2-10) + CR(0.5-2)} \quad (1)$$

where *CR*(2–10) and *CR*(0.5–2) are the count-rates in the hard and soft energy bands, respectively. The source flux in the soft/hard/total energy bands was computed from the measured count-rates. Following the procedure used by Baldi et al. (2002), the *count-rate-to-flux* conversion factors (*CF*) were computed for each of the *MOS* cameras individually using their updated response matrices, combined with the effective exposure times of each pointing. As a model spectrum we assumed an absorbed power-law with photon index $\Gamma = 1.7$, i.e. a typical AGN spectrum, and a hydrogen column density $N_H = 1.3 \times 10^{21} \text{ cm}^{-2}$, i.e. the value measured in the direction of 1E1207.4–5209.

In the following sub-section, we report basic statistics on the more important catalogue parameters, like the source *S/N* ratio, the total *CR*, and the *HR* relative to the whole observation set. In the last sub-section we also present the $\log N - \log S$ distribution built from the sources in our serendipitous catalogue.

3.2. Catalogue statistics

The histogram of the source *signal-to-noise* (*S/N*) ratio distribution is shown in Fig. 2 in the soft, hard, and total energy bands. In the total energy band (0.3–8 keV) the distribution peaks at *S/N* = 4–6 (Fig. 2, top). However, thanks to the long effective integration time and to the increased count statistics, a large fraction (~40%) of sources are also detected with *S/N* \geq 10. Very few sources are detected with *S/N* \geq 20. In the hard energy band (2–10 keV) sources are generally detected with a quite low *S/N* ratio, with the peak of the distribution at 4 (Fig. 2, middle) and with only ~20% of the sources detected with *S/N* \geq 10. On the other hand, sources are detected with the best *S/N* ratio in the soft energy band (0.5–2 keV), with the distribution peaking at 6–8 (Fig. 2, bottom), and with a much larger fraction of sources (~35%) detected with *S/N* \geq 10. This is most

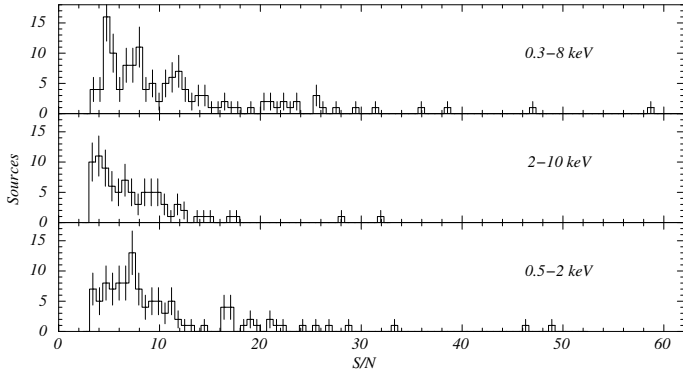


Fig. 2. Histogram of the S/N ratio distribution in the energy bands 0.3–8 keV, 2–10 keV, and 0.5–2 keV (top to bottom) for the serendipitous X-ray sources.

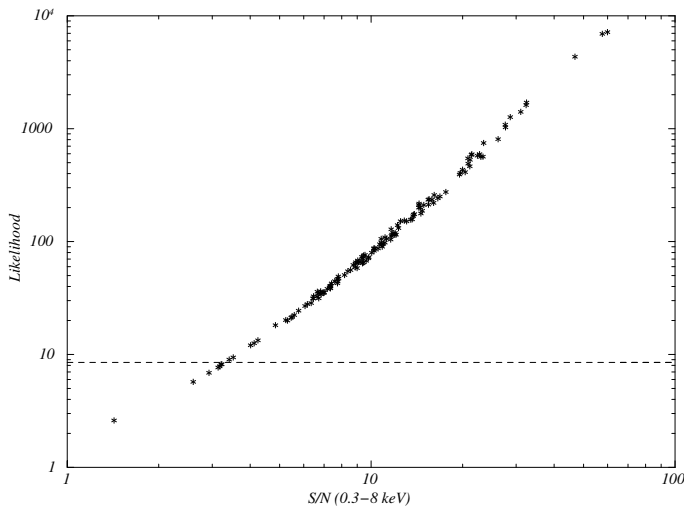


Fig. 3. Correlation between the detection likelihood and the S/N ratio, both computed in the 0.3–8 keV energy band, for the serendipitous sources. The dashed line corresponds to the detection likelihood threshold ($-\ln P = 8.5$) in the 0.3–8 keV band. Sources below this line are included because they are above the detection threshold in at least one of the other two energy bands (see Sect. 2.4).

likely ascribed to the better sensitivity of the *MOS* cameras at low energies.

In Fig. 3 we show, as a reference, the correlation between the source detection likelihood $-\ln P$ and the source S/N ratio in the total energy band 0.3–8 keV. As expected, the detection likelihood increases with the S/N ratio, without any large scatter or change of slope at the two extremes of the distribution.

The histograms of the source *count-rate* (CR) distribution for the two coarse soft (0.5–2 keV) and hard (2–10 keV) energy bands are shown in Fig. 4. The peak of the CR distribution is at 6.31 cts s^{-1} ($\log CR = -3.2$) and 2.81 cts s^{-1} ($\log CR = -3.55$) in the soft and hard energy bands, respectively. As seen from the histograms, only a few X-ray sources have a relatively high count-rate ($\log CR \geq -3$), and thus lower statistical errors, in either of the two energy bands. For this reason, only these sources with count-rate variations measured over the 2001/2002 and 2005 observation subsets can be considered indicative of a statistically significant long term variability (Sect. 4.2).

The histogram of the HR distribution is shown in Fig. 5. Most of the sources have $-0.5 \leq HR \leq 0$ and a large fraction has $HR \sim -1$. This suggests that a significant fraction of the X-ray source population is characterised by rather soft spectra,

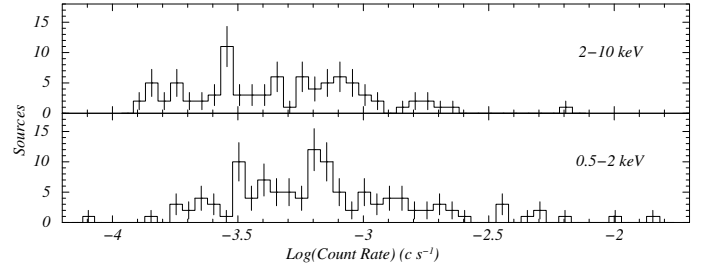


Fig. 4. Histogram of the source count-rate distribution in the 2–10 keV and 0.5–2 keV energy bands (top and bottom, respectively).

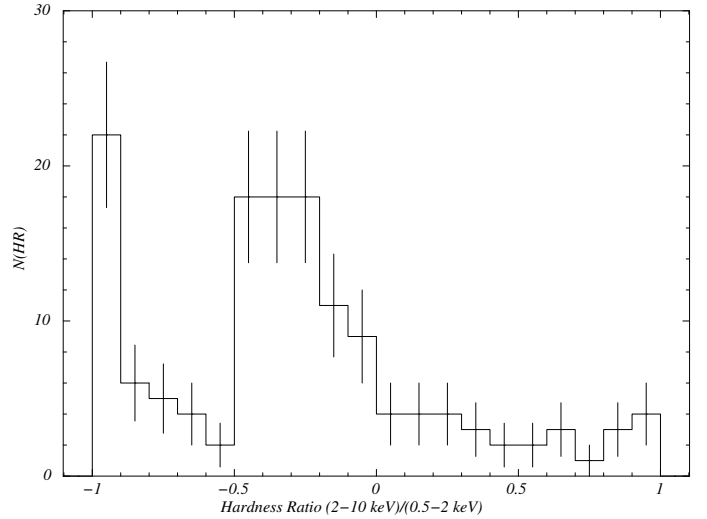


Fig. 5. Histogram of the HR distribution for the serendipitous X-ray sources detected in the 1E1207.4–5209 field.

with no detection in the 2–10 keV energy band. On the other hand, the histogram shows that only few sources have very hard spectra ($HR \approx 1$).

3.3. Flux limit and sky coverage

The actual sky coverage in the various energy ranges was computed by applying the procedure described in Baldi et al. (2002), which is consistent with the standard method used in the *XMM-Newton* Serendipitous Survey (Carrera et al. 2007; Mateos et al. 2008). For each energy band we used the exposure maps of each of the two *MOS* cameras and the background map of the co-added image, as derived in Sect. 2.3, to compute the flux limit map of the whole observation set. To this aim, we applied the *count-rate-to-flux* conversion factors (CF) obtained with the absorbed power-law spectrum described in Sect. 3.1. This gives, for each position on the sky covered by the *MOS* observations, the flux that a source must have in order to be detected with a minimum probability $P = 2 \times 10^{-4}$ (Baldi et al. 2002; Novara et al. 2006). We used the flux limit maps to derive the total sky coverage shown in Fig. 6. This shows that our observations cover a sky area of $\approx 0.15 \text{ deg}^2$, down to X-ray fluxes of $\approx 2 \times 10^{-15}$ and $8 \times 10^{-15} \text{ erg cm}^{-2} \text{ s}^{-1}$ in the energy ranges 0.5–2 and 2–10 keV, respectively.

3.4. Log N –log S distribution

We followed the procedure used by Baldi et al. (2002) to compute the log N –log S distribution built from our serendipitous

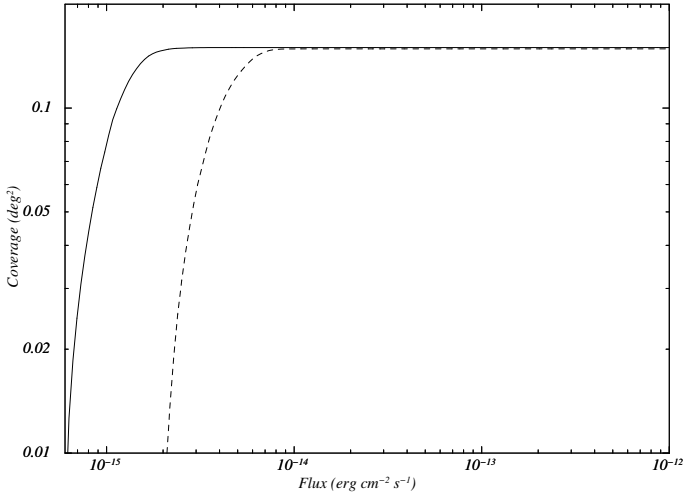


Fig. 6. Sky coverage of the *XMM-Newton* observations, in the soft energy range 0.5–2 keV (solid line) and in the hard energy range 2–10 keV (dashed line).

X-ray sources, and we refer to their paper for further details. Figure 7 shows the cumulative $\log N$ – $\log S$ distribution (asterisks) relative to the soft (0.5–2 keV) and hard (2–10 keV) energy bands (top and bottom panel, respectively). In the soft band the flux limit is $\sim 1 \times 10^{-15}$ erg cm $^{-2}$ s $^{-1}$, corresponding to a maximum source density of ~ 1300 sources deg $^{-2}$, while in the hard energy band it is $\sim 3 \times 10^{-15}$ erg cm $^{-2}$ s $^{-1}$, corresponding to a source density of ~ 700 sources deg $^{-2}$. Both the soft and hard distributions feature an evident change of slope at $S \sim 4 \times 10^{-15}$ and $S \sim 2 \times 10^{-14}$ erg cm $^{-2}$ s $^{-1}$, respectively. We note that a similar turn-over was already observed by [Ebisawa et al. \(2005\)](#) in the *Chandra* observation of the galactic plane, and also in the *XMM-Newton Serendipitous Survey* ([Carrera et al. 2007](#); [Mateos et al. 2008](#)), even if in the latter case the flux breaks are at $S \sim 1 \times 10^{-14}$ erg cm $^{-2}$ s $^{-1}$ in both energy bands. With respect to the results reported by [Mateos et al. \(2008\)](#), we obtain a comparable flux limit in the soft energy band, while in the hard band we obtain a much lower limit. Moreover, in both energy ranges our cumulative source density is higher, since they obtain ~ 600 and ~ 300 sources deg $^{-2}$ in the soft and hard energy ranges, respectively. We note that we used a unique power-law spectral index $\Gamma = 1.7$ to calculate our *CFs* in the two energy ranges, while [Mateos et al. \(2008\)](#) used spectral indexes of 1.9 and 1.6 below and above 2 keV, respectively. However, they showed that differences ≤ 0.3 in the spectral index can imply variations in the $\log N$ – $\log S$ of only 1–2% and of $\leq 9\%$ in the hard and soft bands, respectively. Therefore, we assume that our results are not biased by the used spectral parameters

For comparison, in Fig. 7 we superimposed on our data the lower and upper limits of the $\log N$ – $\log S$ computed by [Baldi et al. \(2002\)](#) at high galactic latitude ($|b| > 27^\circ$). We note that, with respect to our work, they obtained the upper limit $\log N$ – $\log S$ by applying the same detection threshold ($P_{\text{th}} = 2 \times 10^{-4}$) but a larger extraction radius, while the lower limit $\log N$ – $\log S$ was obtained with the same extraction radius but a more constraining threshold value ($P_{\text{th}} = 2 \times 10^{-5}$). In addition, we overplotted the $\log N$ – $\log S$ distributions computed from *Chandra* observations of the galactic plane ([Ebisawa et al. 2005](#)), as well as their 90% confidence limits.

In the soft energy band our $\log N$ – $\log S$ distribution is well above the high-latitude upper limit of [Baldi et al. \(2002\)](#). This means that in our serendipitous survey we detected a

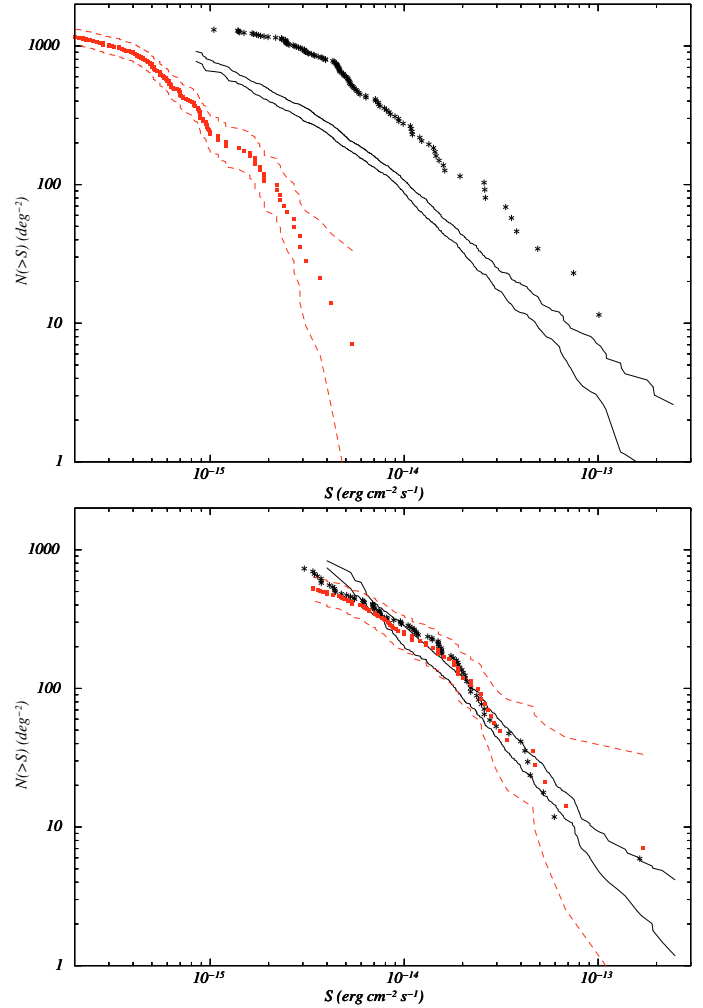


Fig. 7. Cumulative $\log N$ – $\log S$ distributions of the serendipitous sources detected in the 1E1207.4–5209 field in the soft (0.5–2 keV, top) and hard (2–10 keV, bottom) energy ranges (asterisks). The black solid lines mark the upper and lower limits obtained by [Baldi et al. \(2002\)](#) in the same energy ranges but at higher galactic latitudes. The red filled squares and the red dashed lines represent the distributions and the limits measured by *Chandra* in the Galactic plane ([Ebisawa et al. 2005](#)), respectively.

large sample of galactic sources which are missed not only at higher latitudes but also in the Galactic plane, due to the high amount of interstellar absorption. However, we note that our $\log N$ – $\log S$ distribution flattens at low X-ray fluxes with respect to, e.g. that shown in Paper I, with a clear break at $S \sim 4 \times 10^{-15}$ erg cm $^{-2}$ s $^{-1}$. This trend is due to the tighter criteria (see Sect. 2.4) that we adopted to validate the detection of serendipitous sources, together with the improved *SAS* detection algorithm which minimises the number of spurious sources detected in regions of diffuse emission, like those associated with the SNR PKS 1209–51. This results in a lower number of sources detected in the soft energy band, which is now 114 with respect to the 135 reported in Paper I. Indeed, we identified the missing sources with the faintest ones reported in Paper I, which explains the reduced number of sources at the low flux end of the new $\log N$ – $\log S$ distribution. Our $\log N$ – $\log S$ distribution is also well above the Galactic plane $\log N$ – $\log S$ distribution (the red points in Fig. 7), which means that we detected a significant fraction of extra-galactic sources which are missed at low galactic latitude.

In the hard energy band, our $\log N - \log S$ distribution is very close to that observed in the Galactic plane. With respect to the high latitude limits, our distribution shows a slight excess in the flux range $1-2 \times 10^{-14}$ erg cm $^{-2}$ s $^{-1}$, possibly due to the contribution of a fraction of Galactic sources which are missed at higher latitudes. On the other hand, the faintest end of our distribution is below the high latitude lower limit. We attribute this result to the tight criteria that we used to validate the detected source, which implies the rejection of the faintest objects.

4. The bright source sample

4.1. Spectral analysis

Although the *HR* provides qualitative information on the source X-ray spectra, it is not a robust spectral classification. As we mentioned in Paper I, at least 500 total *MOS* counts (i.e. *MOS1* + *MOS2* events) over the whole detector energy range are required to discriminate thermal X-ray spectra from non-thermal ones. Following this criterion, we selected the 40 brightest sources (Fig. 8) in our serendipitous source catalogue which total >500 counts. This bright source sample obviously includes the 24 brightest sources similarly selected in Paper I. For each of the two *MOS* cameras we extracted the source event list using extraction radii of 20''–35''. Background regions were selected near the source positions, with a radius three times that used for the source extraction. All spectra extracted from the event lists were rebinned in order to have a minimum of 30 counts per energy bin, which is required to precisely apply the χ^2 minimization fitting technique. For each of the two *MOS* spectra we generated ad hoc response matrices and ancillary files using the *SAS* tasks *rmfgen* and *arfgen* with both thermal and non-thermal spectral models. We took into account the different size of the source and background extraction areas and renormalized the background count-rate, then we simultaneously fitted the two spectra of each source, forcing common parameters and allowing only for a cross-normalization factor to account for the different instrument efficiency. We considered four spectral models: *power-law*, *bremsstrahlung*, *black-body*, and *mekal*. In all cases, the hydrogen column density N_H was left as a free parameter. For each emission model we computed the 90% confidence level error on both the N_H and on the spectral parameters, i.e. the plasma temperature or the photon-index. As seen from Table 5, we found that 14 sources were best fitted by a *power-law* model (Fig. 9), 2 by a *bremsstrahlung* model, and 3 by a *mekal* model (Fig. 10). For 16 of the remaining 20 sources, at least two different models provided an acceptable fit with a comparable value of the χ^2_ν . For 5 sources it was not possible to obtain acceptable results with single-component spectral model. This is, e.g. the case for source #239 (XMMU J121029.0–522148), the proposed Seyfert-2 galaxy identified in Paper I, which is characterised by a complex spectral model as discussed in Sect. 4.3.

4.2. Time variability

In order to investigate possible long term variability between exposures we selected from our bright source sample 33 X-ray sources that we detected in both the 2001/2002 and 2005 observation subsets (see Table 1) and in the total (0.3–8 keV) energy band, chosen as a reference. For each source we computed the count-rate variation ΔCR between the two observation subsets. Figure 11 (top) shows the relative *CR* variation with respect to the first observation subset plotted as a function of the source *S/N* ratio. As seen, a few sources

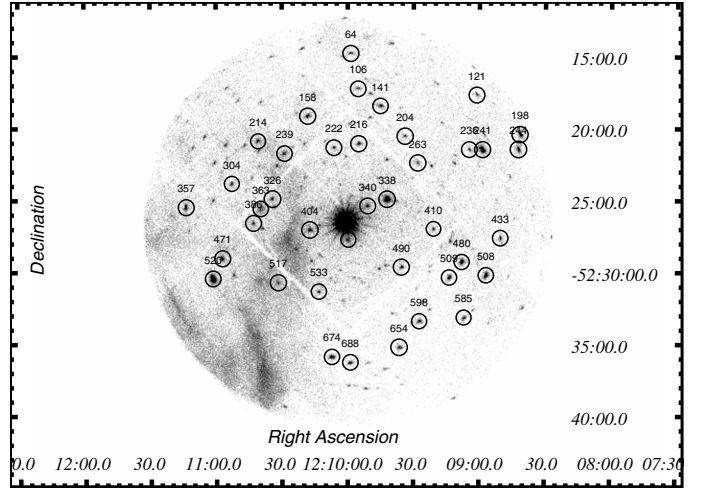


Fig. 8. Processed *XMM-Newton* EPIC/*MOS* 0.3–8 keV band image of the 1E1207.4–5209 field with the position of the 40 brightest serendipitous sources over plotted. Sources are labelled according to the numbering used in Table 5. Circles are drawn only to highlight the X-ray source positions and their size do not correspond to their actual positional errors.

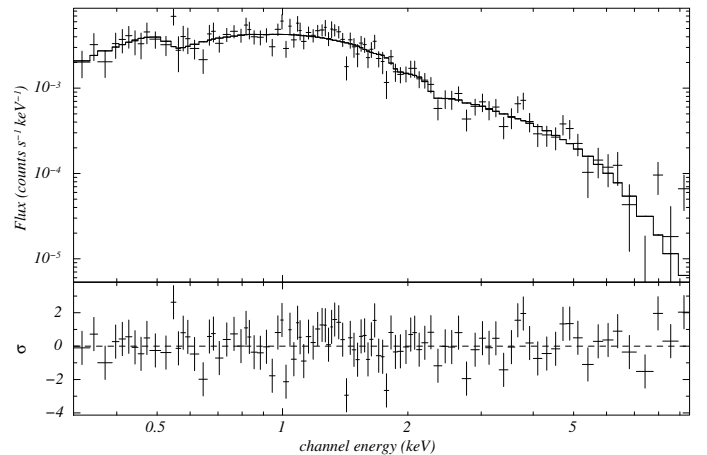


Fig. 9. Unbinned non-thermal spectrum of source #338 (XMMU J120942.1–522458) with the best-fit *power-law* model.

show non-zero long term variability which is mostly within 30% but can be up to $\sim 200\%$. Figure 11 (bottom) shows the absolute *CR* variation $|\Delta CR|$ divided by its associated error $\delta(\Delta CR)$ plotted as a function of the source *S/N* ratio. As seen, 10 X-ray sources show evidence of variability at more than 3σ . For 6 of them, i.e. source #326 (XMMU J121034.6–522457), #404 (XMMU J121017.5–522706), #410 (XMMU J120921.0–522700), #471 (XMMU J121057.3–522905), #480 (XMMU J120908.1–522918), and #520 (XMMU J121101.5–523030), the variability is at the $\geq 5\sigma$ level. We thus regard these sources as likely transients. Among them, source #326 (XMMU J121034.6–522457) features the strongest variability ($\sim 200\%$, $\approx 7\sigma$), followed by source #410 (XMMU J120921.0–522700) whose variability is of $\sim 100\%$ but is significant only at the $\sim 5\sigma$ level. On the other hand, sources #480 (XMMU J120908.1–522918) and #520 (XMMU J121101.5–523030) feature a variability of only $\sim 15-25\%$, although detected with the highest significance ($\approx 10\sigma$). This is obviously due to the fact that both sources were detected with the highest *S/N* ratio (≥ 30).

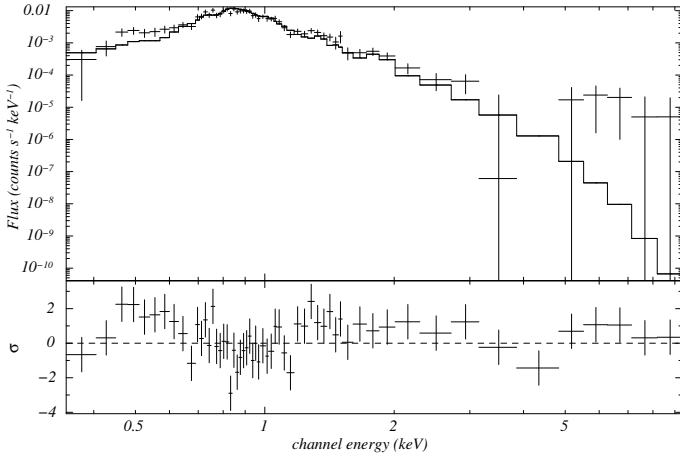


Fig. 10. Unbinned thermal spectrum of source #241 (XMMU J120858.8–522129) with the best-fit *thermal mekal* model.

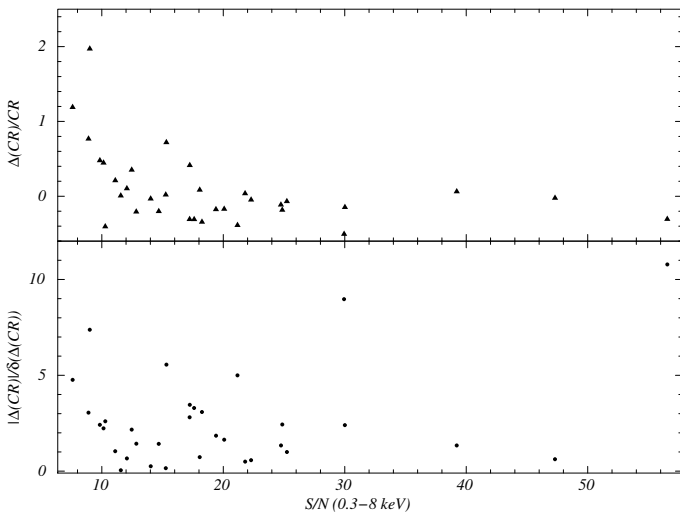


Fig. 11. *Top:* relative CR variation with respect to the first observation subset plotted as a function of the source S/N ratio (filled triangles). *Bottom:* absolute CR variation $|\Delta CR|$ divided by its associated error $\delta(\Delta CR)$ plotted as a function of the source S/N ratio (filled circles).

For all sources in our bright sample, we searched for variability on a shorter time scale, including within exposures, through a light-curve analysis with optimised time binning (1, 5, or 10 ks) and using as a reference only CR measurements relative to the observations with the longest exposure times, i.e. the second and the third observation of the 2002 data-set and the fourth observation of the 2005 data set (Table 1). Of the 6 X-ray sources with $\geq 5\sigma$ possible long term variability, our light-curve analysis does not show evidence of short term variability while it confirms the long term one for all sources but not for source #520 (XMMU J121101.5–523030). This result is not surprising since this source is the one with the lowest relative variation ($\sim 25\%$, see Fig. 11 (top)), which is thus more difficult to recognise if spread on a shorter time scale. None of the remaining 4 X-ray sources with possible long term variability ($\sim 3\text{--}5\sigma$) shows any evidence of short term variability.

For the persistent sources (long term variability $\leq 3\sigma$), we confirm flux variability on time-scales of a few hundred seconds for source #158 (XMMU J121018.4–521911) and of ~ 10 ks for source #338 (XMMU J120942.1–522458), which correspond to

source #72 and #183 of Paper I, respectively. For the remaining sources, we did not find evidence of significant variability on any time scale.

Finally, we also looked for possible periodic time variability. Unfortunately, in this case the low count statistics prevented the detection of any periodic signal at a reasonable significance level.

4.3. The Seyfert-2 galaxy ESO 217-G29

Source #239 (XMMU J121029.0–522148) was originally identified as a new Seyfert galaxy in Paper I (source #127), due to its X-ray spectrum and to its positional coincidence with the galaxy ESO 217-G29, a bright ($R = 14.93$) barred spiral with a spectroscopic redshift of 0.032 (Visvanathan & van den Bergh 1992) also detected in the *Digitised Sky Survey* images. From the merged image (see Sect. 2.3) we have now obtained a total of 821 counts in the energy range 0.3–8 keV for source #239, which is 38% higher with respect to that of the data set used in Paper I. For this reason, we repeated the source spectral analysis in order to achieve a more accurate characterisation of the X-ray spectrum. The spectrum of the source between 1 and 12 keV is complex and cannot be fitted by a single-component model. We thus used the AGN unification model of Antonucci (1993) and Mushotzky et al. (1993)

$$S = A_G[A_{SP}(R_W) + A_T(PL + R_C + GL)]^4$$

where A_G is the galactic absorption ($1.28 \times 10^{21} \text{ cm}^{-2}$), A_{SP} is the absorption related to the AGN host galaxy, R_W is the warm and optically thin reflection component, A_T is the absorption acting on the nuclear emission associated to the torus of dust around the AGN nucleus, PL is the primary power-law modelling the nuclear component, R_C is the cold and optically thick reflection component, and GL is the Gaussian component that models the Fe line at 6.4 keV. For the A_{SP} , A_T , R_C , and GL components the redshift value is fixed at $z = 0.032$ (Visvanathan & van den Bergh 1992).

For both the *MOS1* and *MOS2* spectra we performed the spectral fitting both fixing the redshift z to the literature value of 0.032 and leaving it as a free parameter. In the first case (Fig. 12), the fit yields a $\chi^2_\nu = 0.77$ (33 d.o.f.) but it does not satisfactorily account for the Fe line since the fitted centroid energy of the line is 6.2 keV instead of 6 keV, as actually measured in the unfitted spectrum. Furthermore, the fitted line is not significant with respect to the model continuum. The fit yields an absorption associated with the dust torus (A_T) of $\sim 71.91 \times 10^{22} \text{ cm}^{-2}$, slightly lower than the value reported in Paper I. In the second case (Fig. 13), the fit also yields a $\chi^2_\nu = 0.77$ (32 d.o.f.) with a best-fit redshift value $z = 0.042^{+0.038}_{-0.032}$ which is between the value reported in Paper I ($z = 0.057$) and the literature one of 0.032. The fit with the free z better accounts for the Fe line whose fitted profile is now significant at the 90% confidence level, with a fitted centroid energy of ~ 6.0 keV. The intrinsic absorption associated to the dust torus (A_T) is $\sim 72.16 \times 10^{22} \text{ cm}^{-2}$, very similar to the previous case. All best-fit parameters for the two cases are summarised in the Table 3. The 2–10 keV unabsorbed flux (calculated with *XSPEC*) of the primary nuclear component is $6.59^{+2.13}_{-1.23} \times 10^{-13} \text{ erg cm}^{-2} \text{ s}^{-1}$ and the X-ray luminosity, computed for a redshift of 0.032, is $2.75^{+0.89}_{-0.51} \times 10^{42} \text{ erg s}^{-1}$.

⁴ `wabs*(zwabs*powerlaw + zwabs*(powerlaw + pexrav + zgauss))` in *XSPEC*.

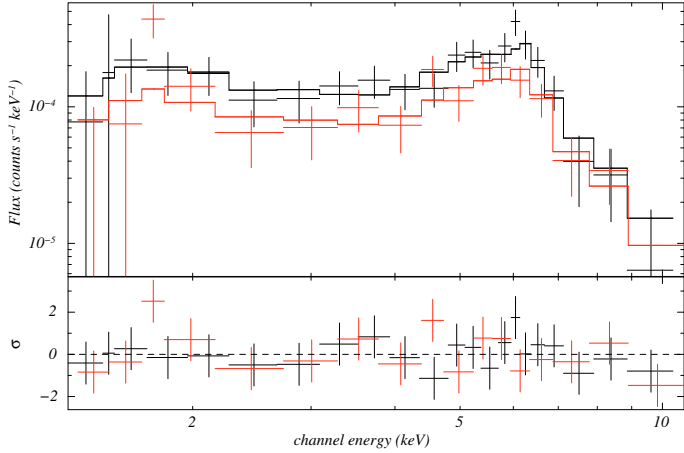


Fig. 12. (Upper panel) The 1.2–12 keV unbinned spectrum of source #239 (XMMU J121029.0–522148) identified with the Seyfert-2 galaxy ESO 217-G29. The fit was performed using the AGN unification model of Antonucci (1993) and Mushotzky et al. (1993) with a fixed redshift of $z = 0.032$. Spectral fits were computed for both the *MOS1* and *MOS2* data (black and red, respectively). (Lower panel) Data-model residuals are shown in units of σ .

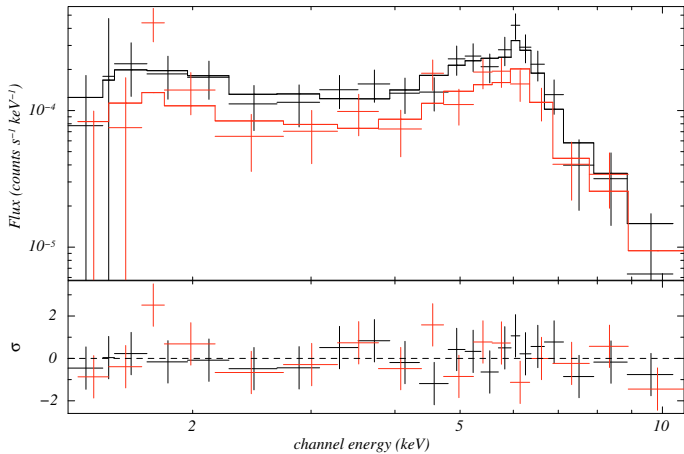


Fig. 13. Same as Fig. 12 but with the best-fit redshift value of $z = 0.042$.

5. Optical observations

5.1. Observation description

In order to search for the optical counterparts of the X-ray sources, we performed follow-up observations (Fig. 14) with the *WFI* mounted at the 2.2 m ESO/MPG telescope at the La Silla observatory (Chile). The *WFI* is a wide field mosaic camera, composed of eight 2048×4096 pixel CCDs, with a scale of $0''.238/\text{pixel}$ and a full field of view of $33'.7 \times 32'.7$, which well matches that of the *EPIC/MOS* cameras. Observations in the *U*, *B*, *V*, *R*, and *I* filters were performed in Service Mode between March 2005 and April 2006 (see Table 4). Unfortunately, scheduling problems prevented observations being executed during the same run. To compensate for the inter chip gaps, pointings were split in sequences of five dithered exposures with shifts of $35''$ and $21''$ in right ascension and declination, respectively. The target field was always observed close to the zenith and nearly always under sub-arcsecond seeing conditions, as measured by the La Silla DIMM seeing monitor.

Table 3. Best-fit parameters for source #239 (XMMU J121029.0–522148), for the optical redshift $z = 0.032$ and for its best-fit value $z = 0.042$.

Component	Parameter	$z = 0.032$ (fix)	$z = 0.042$
A_{SP}	N_{H1}^a	$2.27^{+1.12}_{-0.88}$	$2.27^{+1.12}_{-0.82}$
R_W	Γ	1.9 (fixed)	1.9 (fixed)
	Flux @ 1 keV ^b	$8.84^{+3.25}_{-2.65}$	$8.63^{+1.58}_{-1.87}$
A_T	N_{H2}^a	$71.91^{+16.18}_{-15.24}$	$72.16^{+20.92}_{-15.20}$
PL	Γ	1.9 (fixed)	1.9 (fixed)
	Flux @ 1 keV ^c	$2.28^{+1.17}_{-0.79}$	$2.20^{+0.71}_{-0.41}$
R_C	Γ	1.9 (fixed)	1.9 (fixed)
	Flux @ 1 keV ^c	$2.28^{+1.17}_{-0.79}$	$2.20^{+0.71}_{-0.41}$
GL	$E_{\text{line}}(\text{keV})$	6.4 (fixed)	6.4 (fixed)
	J_{line}^d	$1.02^{+1.32}_{-1.02}$	$1.31^{+1.45}_{-1.26}$
	EQW (eV)	126^{+164}_{-126}	164^{+181}_{-158}
d.o.f.		33	32
χ^2_{ν}		0.77	0.77

^a 10^{22} cm^{-2} ; ^b $10^{-6} \text{ ph cm}^{-2} \text{ s}^{-1} \text{ keV}^{-1}$; ^c $10^{-4} \text{ ph cm}^{-2} \text{ s}^{-1} \text{ keV}^{-1}$; ^d $10^{-6} \text{ ph cm}^{-2} \text{ s}^{-1}$.

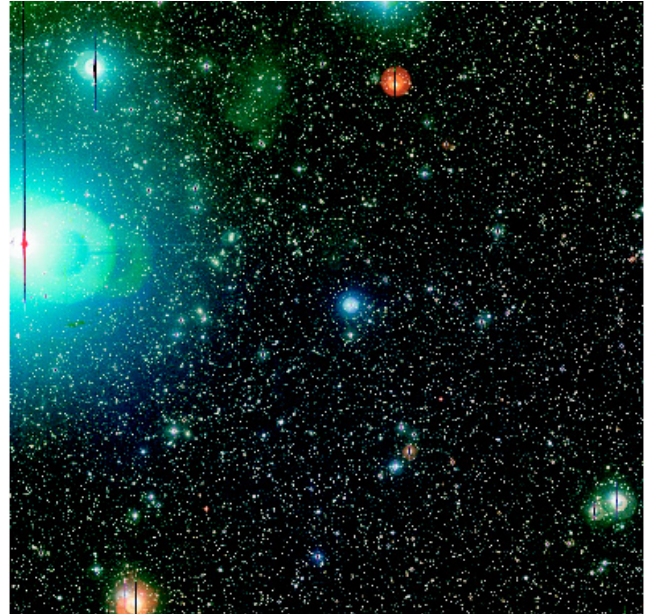


Fig. 14. Composite *VRI* image of the 1E1207.4–5209 field ($34' \times 34'$) taken with the *WFI* at the ESO/MPG 2.2 m telescope. North to the top, east to the left. The effects of the very bright star ρ Cen are clearly visible on the image, with the presence of reflections and bright ghosts.

5.2. Data reduction and calibration

The data reduction of the *WFI* data was performed with the *THELI* pipeline (Erben et al. 2005) which was also used for the reduction of the *WFI* data of La Palombara et al. (2006). Since we followed the same procedures, we refer to the paper of La Palombara et al. (2006) for a more detailed description of the data reduction. Briefly, for each band the individual images were de-biased, flat-fielded, and corrected for the fringing. After the chip-by-chip astrometric calibration (average rms $\sim 0''.3$) computed using a number of well-suited (i.e., bright but not saturated and not detected close to the chip edges) reference stars selected from the *USNO-B1.0* catalogue (Monet et al. 2003), single frames were co-added using a weighted mean to reject cosmic ray hits. A flux-renormalisation to the same relative photometric

Table 4. Summary of the *WFI* optical observations performed by the ESO/MPG 2.2 m telescope.

Date	Filter	Time (s)	Airmass	Seeing
10 Mar. 2005	<i>R</i>	2888.75	1.09	0.99
	<i>I</i>	1999.73	1.15	1.09
01 May 2005	<i>V</i>	2559.09	1.11	0.52
02 May 2005	<i>I</i>	269.42	1.10	0.69
25 Feb. 2006	<i>I</i>	1999.59	1.09	0.86
25 Apr. 2006	<i>B</i>	1999.59	1.09	0.68
	<i>U</i>	2499.59	1.11	0.61

zero-point was applied using the exposure maps produced by the pipeline to account for the uneven exposure produced by the dithering. Since standard star observations were not acquired for all nights and for all bands, we used default *WFI* zero-points⁵ for the photometric calibration, namely 21.96, 24.53, 24.12, 24.43 and 23.37 (in Vega magnitudes) for the *U*, *B*, *V*, *R*, and *I* filters, respectively. A deeper image was then constructed by registering the individual co-added images in the single bands, which was used as a reference for the source detection.

5.3. Source detection

The source extraction was performed on the final co-added single band images by running the *SExtractor* software (Bertin & Arnouts 1996). The source detection was performed after masking the region around the very bright star ρ Cen, a B3V star ($V = 3.9$) that was saturated on all *WFI* images (Fig. 14). This was done to avoid including spurious detections produced by the saturation spikes and to filter out objects whose photometry is polluted by the bright star halo. The masking was applied on the weighted images and, due to the different brightness of the star in the different bands and to the different integration time, the size of the masked region was tailored for each image. The extracted catalogues were checked against the images and the counterparts were visually inspected to make sure that the spurious detections were minimal (less than $\sim 1\%$). Single band optical catalogues were then matched using a matching radius of $0''.2$, i.e. equal to the rms of our astrometric solution, to produce the final *WFI* colour catalogue. The catalogue includes a total of 64 910 sources with at least a detection in one of the five bands (*UBVRI*). Of these, only 15201 have been detected in all bands. For each filter, the limiting magnitude of the colour catalogue was defined as the magnitude of the object fainter than the remaining 99%. This corresponds to *U*-to-*I* limiting magnitudes of 23.25, 24.72, 24.39, 23.97 and 22.72.

5.4. The optical/NIR catalogue

To extend the colour coverage, required for a colour-based classification of the *WFI* sources, we added near infrared (NIR) photometry information in the *J*, *H* and *K* bands by correlating the *WFI* colour catalogue with the *2MASS* catalogue (Skrutskie et al. 2006). The extracted *2MASS* source list in a $40' \times 40'$ region around the 1E1207.4–5209 position was retrieved through the *Vizier* database server and matched with the *WFI* colour catalogue using the IRAF task *tmatch*. A match radius of $0''.5$ was used to account both for the uncertainty on the *WFI* coordinates and on the $\leq 0''.2$ astrometric accuracy of *2MASS*. A total of 6996 *WFI* sources ($\sim 10\%$) have a match with a *2MASS* source and for 5032 of them we have the full *UBVRI*-to-*JHK*

photometry information. The match produced a master optical/NIR catalogue that we used as a reference for the X-ray source identification and for the colour-based object classification. For all sources with an adequate colour-coverage we used the colour-based optical classification technique described in Hatziminaoglou et al. (2002b) and tested in Hatziminaoglou et al. (2002a) and Groenewegen et al. (2002).

6. X-ray vs. optical/NIR catalogues

6.1. Catalogue cross-correlations

In order to identify candidate counterparts to the X-ray sources, we cross-matched our serendipitous X-ray source catalogue with the optical/NIR master catalogue. Thanks to the improved *SAS* task *emldetect*, the coordinates of the X-ray sources were measured with high accuracy. The measured errors vary between $0''.1$ and $1''.5$, depending on the source counts, with an average error of $\sim 0''.7$. These errors, however, substantially reflect the positional accuracy of the X-ray sources with respect to the detector reference frame and do not account for systematic errors. Indeed, the absolute accuracy of these coordinates with respect to the International Celestial Reference Frame (ICRF) is inevitably affected by the precision of the satellite aspect solution. In order to determine the accuracy of the tie of the measured coordinates to the ICRF, we thus cross-matched our X-ray catalogue with the optical/NIR master catalogue. In this way, we found six X-ray sources which have a single, relatively bright (but not saturated) and obvious optical counterpart which is not at the edges of the *MOS* cameras field-of-view (*FOV*). We thus computed the linear transformation between the X-ray and optical coordinates to correct the *MOS* astrometry. Since the astrometry of the *WFI* catalogue is calibrated with USNOB-1.0, which is tied to the ICRF, we are sure that we did not introduce a bias in our procedure. Using the IRAF task *geomap* we found that the X-ray source coordinates are affected by a (radial) systematic astrometric error of $1''.34$, corresponding to the rms of the X-ray-to-optical coordinate transformation⁶. To this, we have to add in quadrature the measured positional statistic error of each source ($0''.1$ – $1''.5$). Therefore, the total uncertainty on the X-ray source position is between $1''.34$ and $2''.01$. The correction to the X-ray coordinates was then applied to all sources of our serendipitous X-ray catalogue with the IRAF task *geoxytran* using the coefficients of the computed X-ray-to-optical coordinate transformation. To account for all other sources of uncertainty, e.g. the $\sim 0''.2$ absolute accuracy (per coordinate) of the *USNO-B1.0* reference frame (Monet et al. 2003), the distortions of the *MOS* cameras, etc., in the X-ray-to-optical cross-correlation we conservatively assumed a more generous matching radius equal to three times the estimated absolute error on the X-ray source coordinates.

6.2. Sources with candidate optical counterparts

After applying the computed correction to the coordinates of the X-ray sources in our serendipitous catalogue (see previous section), we repeated the cross-correlation with the optical/NIR catalogue. After the cross-match we found at least one candidate counterpart for 112 out of the 144 X-ray sources in our serendipitous catalogue (i.e. 78% of the total). However, a total of 195 candidate counterparts were found since we obtained

⁵ <http://www.ls.eso.org/lasilla/sciops/2p2/E2p2M/WFI>

⁶ We note that in Paper I the systematic astrometric error of the X-ray coordinates was $2''.33$, the discrepancy being due to the different counterpart assumed for one of the six X-ray reference sources.

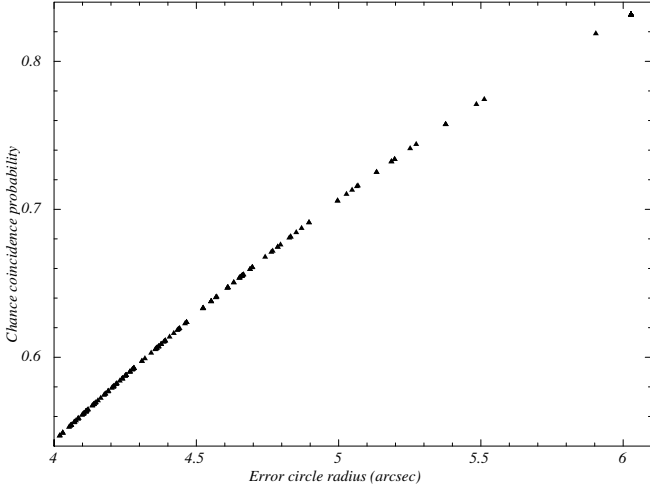


Fig. 15. Chance coincidence probability between an X-ray source and an optical *WFI* source as a function of the matching radius assumed equal to three times the size of the estimated absolute position uncertainty.

multiple matches for several X-ray sources. Due to the relatively deep limiting magnitudes of the *WFI* observations, this is in line with the expectations. We note that in Paper I, where we used the shallower *GSC* catalogue (with only $\sim 16\,000$ optical sources instead of the almost $65\,000$ of the *WFI* catalogue), we found at least one candidate counterpart only for about half of the X-ray sources, even using a more conservative fixed positional uncertainty, hence a more generous cross-matching radius, of $5''$. The choice of assuming a fixed positional uncertainty in Paper I was dictated by the fact that the *SAS* task `em1detect` was failing in providing reliable positional errors.

Due to the contamination of fore/background objects, the result of the cross-matching between the X-ray and optical catalogues is obviously affected by spurious matches. In order to estimate the number of spurious matches, we used the relation $P = 1 - e^{-\pi r^2 \mu}$, where r is the assumed X-ray matching radius and μ is the surface density per square arcsecond of the optical sources, to compute the chance coincidence probability between an X-ray and an optical source (Severgnini et al. 2005). In our case, the *WFI* catalogue provided a total of $64\,910$ sources distributed over an area of about 34×34 arcmin² (i.e. slightly larger than the detector field of view because of the frame dithering). In practice, the useful area is smaller since the $9' \times 7.5'$ region around the bright star ρ Cen was masked after the source extraction. This corresponds to a density of optical sources of $\mu = 0.016$ arcsec⁻², with $r = 4'' - 6''.03$. This yields to a probability of chance coincidence between 55% and 83%, which means that, at our limiting magnitudes, contamination effects cannot be ignored. Thus, it is possible that several of the candidate counterparts are indeed spurious matches. This conclusion is circumstanced by Fig. 15, where we show the dependence of the chance coincidence probability P on the position uncertainty.

6.3. Sources without candidate optical counterparts

For 32 sources in our serendipitous X-ray source catalogue the cross-matching did not produce any candidate optical/NIR counterpart. For seven of them, #357, 380, 387, 230, 173, 181, and 124, the apparent lack of matches is ascribed to the fact that they fall within $\sim 6'$ from the position of the bright star ρ Cen, i.e. in a region which was masked before running the source

detection on the *WFI* images (see Sect. 5.3). For these sources we checked the original unmasked single-band optical catalogues and we visually inspected the *WFI* images to verify the existence of possible counterparts. For all of them we found indeed one or more candidate optical counterparts on the *WFI* images. However, since their flux measurements are highly uncertain, they are useless for a reliable X-ray source identification. This is likely true also for flux measurements taken from, e.g. the *GSC* and *2MASS* catalogues, which were probably affected by the same problem. Thus, although we spotted out their detection as a reference for future follow-up optical observations, these candidate counterparts are not considered in the following analysis. The remaining 25 X-ray sources ($\sim 20\%$ of the total) fall well outside the masked region and are thus the only ones which actually lack a candidate optical/NIR counterpart.

7. X-ray source classification

7.1. The classification scheme

For all X-ray sources we computed the *X-ray-to-optical* flux ratio $\frac{f_x}{f_{opt}}$. We computed the X-ray flux by assuming the best-fit emission model and hydrogen column density or, when none of the tested models gives acceptable spectral fits or no spectral fitting is possible, an absorbed power-law spectrum with photon-index $\Gamma = 1.7$ and $N_H = 1.3 \times 10^{21}$ cm⁻², corresponding to the hydrogen column density measured in the direction of 1E1207.4–5209. The optical flux f_{opt} was computed from the measured magnitudes using the relations reported in Appendix B of La Palombara et al. (2006). The $\frac{f_x}{f_{opt}}$ was mostly computed using the *R*-band magnitude as a reference, because it was the band with the most detections. When no *R*-band magnitude was available for the candidate optical counterpart, we alternatively used the *V*, *B*, *I*, and *U*-band magnitudes (in this order). In order to use the $\frac{f_x}{f_{opt}}$ ratio as a diagnostic for the X-ray source classification, we adopted the scheme proposed by La Palombara et al. (2006), where sources with a $\log(\frac{f_x}{f_{opt}}) > 1$ are likely extra-galactic, while sources with $\log(\frac{f_x}{f_{opt}}) < -1.5$ are likely stars. As a general rule, in cases where two or more different spectral models provide equally acceptable fits to the X-ray spectrum, and thus cause ambiguity in the determination of the $\frac{f_x}{f_{opt}}$ ratio, the source classification was claimed on the basis of the best agreement between the different classification indexes (see below). When no candidate optical counterpart is found within the cross-matching radius we adopted the *R*-band limiting magnitude ($R = 23.97$) to estimate the lower limits on the $\frac{f_x}{f_{opt}}$ ratio.

We then used the combined available multi-wavelength information, i.e. the best-fitting X-ray spectra (or the *HR* for the faintest sources), the measured hydrogen column density N_H , the X-ray-to-optical flux ratio $\frac{f_x}{f_{opt}}$, and the optical/NIR colours of the candidate counterparts, to propose an optical identification and a likely classification for the 112 X-ray sources selected after the catalogue cross-matching (see Sect. 6.2). For the 25 certified sources without candidate optical counterparts (see Sect. 6.3) we used the lower limit on the $\frac{f_x}{f_{opt}}$ ratio to support the proposed classifications based on the source spectrum and N_H . In some cases, X-ray source variability was taken as an important classification index. We note that, due to the quite low declination of our field ($\sim -52^\circ$), no coverage is provided by available large scale radio surveys, like the *NVSS* and *FIRST*, and no candidate

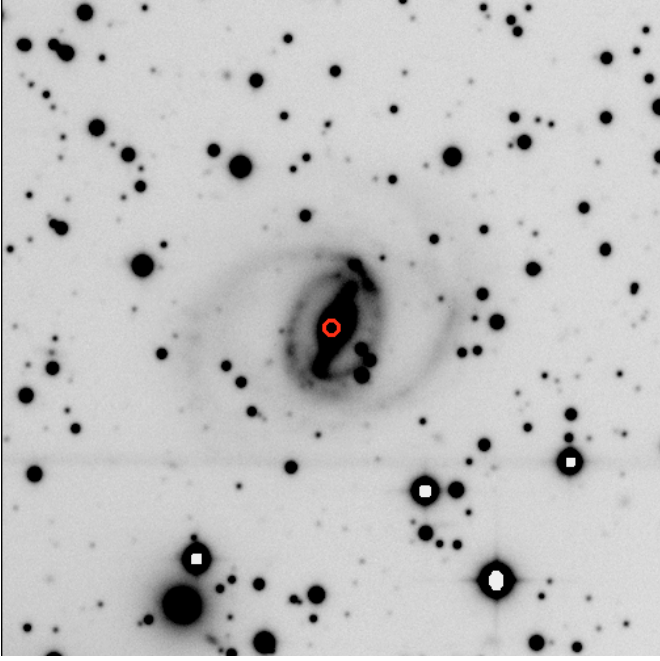


Fig. 16. $2' \times 2'$ *R*-band image of the Seyfert-2 galaxy ESO 217-G29 taken with the *WFI* at the ESO/MPG 2.2 m telescope. The position of the X-ray source #239 (XMMU J121029.0–522148) is marked with the red circle ($1''.38$ radius) and coincides with the ESO 217-G29 nucleus.

radio source counterpart could be identified which could provide a further classification evidence.

7.2. Brightest X-ray sources

We first evaluated the classification of the X-ray sources in our bright sub sample (see 4), for which the relatively accurate determination of the source spectrum and N_{H} represent already an important piece of evidence. In addition, for most of them the optical candidate counterparts are expected to be bright enough to be detected in nearly all the passbands, and thus to have a more reliable colour-based classification.

As mentioned in Sect. 4.3, source #239 (XMMU J121029.0–522148) was already identified in Paper I as a Seyfert-2 galaxy, positionally coincident with the galaxy ESO 217-G29. The positional coincidence is further strengthened by our updated X-ray coordinates $\alpha_{J2000} = 12^{\text{h}}10^{\text{m}}29.01^{\text{s}}$, $\delta_{J2000} = -52^{\circ}21'48''.1$ (after applying the astrometric correction, see Sect. 6.1). The association of source XMMU J121029.0–522148 with the galaxy ESO 217-G29 is evident in our *WFI* images (see Fig. 16), which clearly resolve the galaxy structure (nucleus, bar, and spiral arms) and show that the source position is clearly coincident with the bright nucleus. Strangely enough, the cross-correlation with the *WFI* catalogue yields a candidate optical counterpart which is at $3''.37$ from the nominal X-ray source position. This is an error of *SExtractor*, the software used to run the source detection on the *WFI* images, which did not correctly resolve the nucleus of the galaxy. We thus discarded the flux of the galaxy computed by *SExtractor* and we assumed an *R*-band magnitude of 14.93, as reported in *Simbad*. From the computed X-ray flux (see Sect. 4.3) we thus derived an X-ray-to-optical flux ratio $\frac{f_{\text{X}}}{f_{\text{opt}}} = 0.166$, in agreement with the expectations for a low-luminosity Seyfert-2 galaxy.

In Table 5 we listed all the candidate counterparts to the other 39 X-ray sources of our bright sample (see Sect. 4). 32 of

them ($\sim 82\%$) have at least one optical candidate counterpart. In particular, for 12 X-ray sources ($\sim 27\%$) the cross-matching produced more than one optical candidate counterpart. For each of the optical candidate counterparts (either single or multiple) we reported both their magnitudes (in one reference passband) and their $\frac{f_{\text{X}}}{f_{\text{opt}}}$ ratios (computed for the assumed X-ray spectral model). The proposed classification, reported in Table 5, is considered virtually secured when best agreement is found between the different classification indexes, i.e. the X-ray source spectrum and the hydrogen column density N_{H} , on one side, and the colour-based classification and $\frac{f_{\text{X}}}{f_{\text{opt}}}$ ratio of the optical candidate counterpart, on the other one. For simplicity, we considered only two main X-ray source classes, i.e. *STELLAR* and *AGN*: in the first class we include the standard galactic sources with a soft, mainly thermal spectrum and low X-ray/optical flux ratio, while in the second class we include extra-galactic sources with a hard, likely non-thermal spectrum and high X-ray/optical flux ratio. None of our X-ray sources is associated with cluster of galaxies or with non-active galaxies. We flagged cases where the source classification is likely, but not secured, or uncertain because of one or more inconsistencies between the different classification indexes. To this aim, we devised the classification flag *a* when the source classification is likely but not secured by the identification of its optical counterpart, since the candidate optical counterpart is unclassified, or poorly classified, or undetected. Moreover, when compelling evidence is lacking we consider the source classification as uncertain with the following classification flags: *b* when the best-fit N_{H} value is too low for AGNs and too high for stars; *c* when the X-ray spectrum is not in agreement either with the *X-ray-to-optical* flux ratio or with the colour-based classification of the optical candidate counterparts; *d* when the source X-ray spectrum is not unambiguously determined, and/or the spectral parameters have large errors. Of course, multiple flags were assigned when different cases apply.

Following a decision-tree approach, we thus proposed a virtually secure or likely classification for 15 of the 39 brightest X-ray sources (36% of the total). According to our classification scheme, we proposed that these 15 sources are active galactic nuclei (AGNs). These sources have all a clear, or generally most likely, *power-law* X-ray spectrum, relatively high N_{H} , and 6 of them have an optical candidate counterpart identified with a QSO, with a consistent $\frac{f_{\text{X}}}{f_{\text{opt}}}$ ratio. For example, we classified source #216 (XMMU J120955.1–522105) as an AGN, without any flag, because of its *power-law* spectrum and N_{H} , and because its candidate optical counterparts is classified as QSO. We thus considered the classification of these 6 sources as secured. Three sources, i.e. #304 (XMMU J121052.9–522354), #326 (XMMU J121034.6–522457), and #517 (XMMU J121031.9–523046), have no optical candidate counterpart, while other sources, i.e. #520 (XMMU J121101.5–523030), #471 (XMMU J121057.3–522905), and #533 (XMMU J121013.2–523123), have a candidate optical counterpart but for which no colour-based classification is possible. However, their *power-law* X-ray spectra, N_{H} , and the constraints on the $\frac{f_{\text{X}}}{f_{\text{opt}}}$ ratio, suggest that they are AGNs. Furthermore, two of them, i.e. #326 (XMMU J121034.6–522457) and #520 (XMMU J121101.5–523030), also feature a significant long term X-ray variability (see Sect. 4.2), which reinforces their classification as AGNs. We thus classified these five sources as AGNs and we flagged them as *a* because of the lack of a possible, or unambiguous, optical identification.

Table 5. Main characteristics of the 39 brightest sources. The sources are sorted by decreasing count number.

(1)	(2)	(3)	(4)	(5)	(6)	(7)	(8)	(9)	(10)	(11)	(12)	(13)
SRC	NAME	cts	Model	N_H (10^{21} cm^{-2})	Γ/kT (-keV)	χ^2_ν	D_{X0} (arcsec)	MAG (mag)	OPTICAL FILTER	$\frac{f_{\text{opt}}}{f_{\text{opt}}}$ (\log_{10})	COUNTERPART CLASS	X-RAY SOURCE CLASS
520	XMMU J121101.5-523030	6464	wabs(pow)	$2.2^{+0.4}_{-0.3}$	$1.97^{+0.12}_{-0.11}$	1.07	2.71	19.68	R	0.39	-	AGN ^a
338	XMMU J120942.1-522458	5611	wabs(pow)	$1.1^{+0.3}_{-0.3}$	$1.98^{+0.12}_{-0.11}$	1.15	2.99	19.43	R	0.15	QSO	AGN
241	XMMU J120858.8-522129	3829	wabs(mekal)	$1.4^{+0.6}_{-0.6}$	$0.62^{+0.02}_{-0.02}$	1.63	3.07	13.71	V	-2.11	-	STAR ^{a,c}
508	XMMU J120857.1-523014	2287	wabs(brem)	$2.9^{+0.8}_{-0.8}$	$0.28^{+0.07}_{-0.54}$	1.81	3.14	16.25	R	-1.55	-	STAR ^{a,c}
			wabs(bbody)	$1.0^{+0.9}_{-0.6}$	$0.17^{+0.02}_{-0.02}$	1.72						
480	XMMU J120908.1-522918	2146	wabs(pow)	$1.2^{+0.5}_{-0.5}$	$1.92^{+0.19}_{-0.16}$	0.90	2.42	19.36	R	-0.06	QSO	AGN
198	XMMU J120841.6-522026	1976	wabs(pow)	$0.1^{+0.02}_{-0.04}$	$1.85^{+0.22}_{-0.19}$	0.95	3.38	20.14	R	0.46	QSO	AGN ^b
674	XMMU J121007.2-523555	1631	wabs(pow)	$0.8^{+0.5}_{-0.5}$	$1.71^{+0.14}_{-0.17}$	1.13	3.28	21.71	R	1.10	MS M3-M4	AGN ^b
244	XMMU J120842.5-522128	1603	wabs(pow)	<0.08	$1.66^{+0.20}_{-0.22}$	0.82	3.70	21.97	V	1.22	QSO	AGN ^{a,b}
357	XMMU J121113.8-522532	1488	wabs(brem)	$4.4^{+1.8}_{-1.5}$	$0.26^{+0.10}_{-0.10}$	1.73	3.33	21.02	R	0.75	MS A7-WD	uncl ^c
			wabs(bbody)	$2.5^{+1.9}_{-1.4}$	$0.16^{+0.03}_{-0.03}$	1.75	-	-	-	-	-	(see note 7)
471	XMMU J121057.3-522905	1353	wabs(pow)	$9.4^{+0.4}_{-2.8}$	$2.12^{+0.32}_{-0.33}$	1.48	3.92	20.11	R	-0.10	-	AGN ^a
			wabs(mekal)	$8.9^{+3.4}_{-2.8}$	$3.63^{+2.06}_{-1.06}$	1.42	3.60	20.42	R	0.03	-	
			wabs(brem)	$7.6^{+2.8}_{-2.0}$	$4.27^{+3.28}_{-1.53}$	1.48	2.67	20.11	R	0.00	WD	AGN ^{b,c}
509	XMMU J120913.8-523023	1319	wabs(pow)	$0.9^{+0.3}_{-0.3}$	$1.97^{+0.17}_{-0.17}$	0.89	3.66	15.84	R	-1.92	Sbc-vB2	uncl ^c
			wabs(brem)	$0.3^{+0.4}_{-0.4}$	$4.27^{+2.57}_{-1.24}$	0.96	-	>23.97	R	>1.24	-	AGN ^{a,b}
426	XMMU J121000.0-522747	1271	wabs(pow)	$0.1^{+0.6}_{-0.0}$	$1.64^{+0.16}_{-0.18}$	2.15	3.81	20.17	V	0.00	-	AGN ^{a,b}
340	XMMU J120951.1-522525	1131	wabs(pow)	$0.4^{+0.7}_{-0.0}$	$1.79^{+0.21}_{-0.28}$	0.87	3.46	15.47	R	-2.51	MS K3-K2	STAR ^b
			wabs(brem)	<0.4	$5.34^{+4.37}_{-2.10}$	0.93	3.00	22.33	R	0.33	QSO	AGN
598	XMMU J120927.4-523326	1128	wabs(pow)	$0.9^{+0.6}_{-0.5}$	$2.07^{+0.16}_{-0.21}$	0.92	3.39	18.74	R	-0.78	QSO	AGN
404	XMMU J121017.5-522706	1119	wabs(mekal)	$5.3^{+1.1}_{-1.2}$	$0.63^{+0.06}_{-0.06}$	1.39	3.58	22.27	R	0.63	MS M2	AGN
158	XMMU J121018.4-521911	1090	wabs(brem)	$2.8^{+1.5}_{-1.2}$	$0.28^{+0.11}_{-0.08}$	1.38	4.04	16.49	R	-1.82	MS M3	AGN ^b
490	XMMU J120935.6-522940	1058	wabs(pow)	$4.5^{+2.6}_{-1.5}$	$2.46^{+0.64}_{-0.45}$	1.09	3.00	22.33	R	0.33	QSO	AGN
			wabs(brem)	$3.0^{+1.9}_{-1.3}$	$2.46^{+1.93}_{-0.84}$	1.10					-	
			wabs(bbody)	$0.2^{+1.9}_{-0.0}$	$0.57^{+0.09}_{-0.09}$	1.29	3.39	18.74	R	-0.78	QSO	AGN
216	XMMU J120955.1-522105	1033	wabs(pow)	$1.5^{+0.8}_{-0.9}$	$2.06^{+0.37}_{-0.29}$	1.25	3.58	22.27	R	0.63	MS M2	AGN
585	XMMU J120906.9-523310	980	wabs(pow)	$1.8^{+0.8}_{-0.8}$	$1.96^{+0.21}_{-0.25}$	1.01	3.79	21.76	R	0.58	QSO	AGN
			wabs(brem)	$1.0^{+0.5}_{-0.5}$	$4.46^{+3.38}_{-3.08}$	1.05	2.53	19.51	R	-0.32	QSO	AGN
141	XMMU J120945.2-521828	959	wabs(pow)	$0.1^{+0.5}_{-0.0}$	$1.48^{+0.28}_{-0.18}$	1.38	3.46	21.05	R	0.44	QSO	AGN ^b
688	XMMU J120959.0-523618	946	wabs(pow)	$2.3^{+1.0}_{-0.9}$	$1.94^{+0.22}_{-0.29}$	0.80	2.18	22.00	V	0.57	-	AGN ^a
			wabs(brem)	$1.5^{+1.0}_{-0.6}$	$4.69^{+4.41}_{-1.58}$	0.81	3.63	22.53	V	0.79	-	AGN ^a
654	XMMU J120936.5-523515	888	wabs(pow)	$1.3^{+0.1}_{-0.0}$	$2.08^{+0.69}_{-0.55}$	1.63	3.38	22.66	R	0.89	-	AGN ^a
433	XMMU J120850.5-522738	818	wabs(brem)	$2.2^{+0.2}_{-0.1}$	$0.47^{+0.21}_{-0.17}$	1.69	2.27	16.63	R	-1.77	MS K5-M0	STAR ^b
214	XMMU J121040.9-522055	785	wabs(pow)	<0.3	$1.92^{+0.24}_{-0.21}$	1.76	-	>23.97	R	>1.39	-	AGN ^{a,b}

Table 5. continued.

(1) SRC	(2) NAME	(3) cts	(4) Model	(5) N_{H} (10^{21} cm^{-2})	(6) Γ/kT (-/keV)	(7) χ^2_{ν}	(8) D_{Xo} (arcsec)	(9) MAG (mag)	(10) OPTICAL FILTER	(11) $\frac{F_{\text{opt}}}{F_{\text{Xo}}}$ (\log_{10})	(12) OPTICAL COUNTERPART CLASS	(13) X-RAY SOURCE CLASS
363	XMMU J121039.9-522538	773	wabs(mekal)	$1.7^{+1.1}_{-1.4}$	$0.53^{+0.10}_{-0.06}$	2.70	3.06	14.22	R	-2.74	-	STAR ^{a,b}
304	XMMU J121052.9-522354	699	wabs(pow)	$2.4^{+2.6}_{-1.4}$	$1.56^{+0.38}_{-0.28}$	1.41	-	>23.97	R	>1.52	-	AGN ^a
326	XMMU J121034.6-522457	694	wabs(pow)	$7.8^{+5.0}_{-3.7}$	$1.30^{+0.30}_{-0.31}$	1.31	-	>23.97	R	>1.44	-	AGN ^a
372	XMMU J120950.5-522613	618	wabs(bbody)	$0.9^{+0.3}_{-0.0}$	$1.26^{+0.24}_{-0.18}$	1.33	-	>23.97	R	>1.40	-	STAR ^d
386	XMMU J121043.1-522638	605	wabs(brem)	<0.05	$0.25^{+0.03}_{-0.03}$	1.26	5.43	20.57	R	-0.55	MS K4	-
236	XMMU J120904.8-522129	551	?	<0.05	$0.73^{+0.27}_{-0.24}$	1.13	2.59	23.86	U	0.82	-	uncl
222	XMMUJ121006.3-522122	540	wabs(pow)	$2.2^{+1.7}_{-1.6}$	$1.89^{+0.66}_{-0.23}$	0.94	2.41	18.47	R	-0.96	-	AGN ^a
204	XMMU J120934.1-522034	535	wabs(bbody)	<0.9	$0.61^{+0.13}_{-0.11}$	1.21	3.50	22.42	R	0.65	-	AGN ^b
410	XMMU J120921.0-522700	535	wabs(pow)	$0.5^{+1.5}_{-0.0}$	$2.38^{+0.93}_{-0.51}$	1.06	3.36	20.44	R	-0.50	QSO	AGN ^b
121	XMMU J120901.3-521741	533	wabs(brem)	<0.7	$1.70^{+1.30}_{-0.73}$	1.04	2.18	19.76	R	-0.77	QSO	uncl ^c
106	XMMU J120955.3-521716	522	wabs(brem)	$6.4^{+5.6}_{-3.1}$	$4.35^{+8.50}_{-2.53}$	1.56	3.48	21.39	R	0.21	MS F5	uncl ^c
263	XMMU J120928.2-522225	515	wabs(pow)	$8.9^{+0.8}_{-4.6}$	$2.18^{+1.02}_{-0.37}$	1.53	-	>23.97	R	0.23	-	AGN ^{a,d}
64	XMMU J120958.7-521449	512	wabs(bbody)	$0.7^{+4.7}_{-0.0}$	$0.77^{+0.18}_{-0.19}$	1.72	-	-	-	0.14	-	uncl
517	XMMU J121031.9-523046	508	wabs(pow)	$4.6^{+0.5}_{-0.3}$	$2.15^{+0.58}_{-0.69}$	1.54	-	-	-	>0.88	-	AGN
533	XMMU J121013.2-523123	499	wabs(bbody)	$0.2^{+0.3}_{-0.0}$	$0.65^{+0.18}_{-0.18}$	1.75	-	-	-	-	-	uncl
			?	$4.8^{+0.4}_{-2.4}$	$1.73^{+0.57}_{-0.41}$	1.16	3.75	21.87	R	0.49	QSO	uncl
			?	-	-	-	2.95	19.96	R	-0.18	QSO	AGN
			?	-	-	-	2.13	23.53	R	1.24	-	uncl
			?	-	-	-	0.86	22.46	R	0.49	-	uncl
			?	-	-	-	2.19	22.51	R	0.51	QSO	AGN ^{a,b}
			?	$0.2^{+0.1}_{-0.2}$	$1.84^{+0.79}_{-0.46}$	1.25	3.93	22.09	R	0.34	MS M2.5	AGN ^a
			?	$1.7^{+0.4}_{-0.0}$	$1.78^{+0.86}_{-0.58}$	0.77	3.04	22.14	R	0.36	MS K7-K5	AGN ^a
			?	<1.6	$0.63^{+0.18}_{-0.14}$	0.98	1.72	23.46	R	1.26	-	AGN ^a
			?	$3.4^{+0.3}_{-0.2}$	$2.05^{+0.30}_{-0.44}$	1.43	-	>23.97	R	>0.73	-	AGN ^a
			?	<1.4	$0.65^{+0.11}_{-0.10}$	1.63	3.65	20.66	U	-0.18	-	AGN ^a
			?	<1.4	$0.65^{+0.11}_{-0.10}$	1.63	3.28	16.18	R	-2.25	-	AGN ^a

Key to table – Col. (1): source ID number. Column (2): catalogue name. Column (3): source total counts (in the 0.3–8 keV energy range). Column (4): best-fit emission model(s); the symbol “uncl” indicates that none of the tested single-component models provided an acceptable fit. Column (5): best-fit hydrogen column density with the associated 90% confidence errors. Column (6): best-fit photon-index or plasma temperature (for a power-law or a thermal emission model, respectively) with the associated relevant 90% confidence level error. Column (7): best-fit reduced chi-square. Column (8): angular distance between the X-ray source position and its optical candidate counterpart (if any). The most likely optical counterpart are listed first. Column (9): magnitude of the optical candidate counterpart or $R \geq 23.97$ upper limit if no candidate counterpart is found. Column (10): optical filter; if the optical candidate counterpart has no R -band magnitude we considered the V , B , I and U -band magnitudes in this order. Column (11): logarithmic values of the X-ray-to-optical flux ratio; the optical flux is based on the magnitudes in Col. (9) while the X-ray flux is based on the best-fit model or, when no model is acceptable, on a power-law spectrum with photon-index $\Gamma = 1.7$ and hydrogen column density $N_{\text{H}} = 1.3 \times 10^{21} \text{ cm}^{-2}$, corresponding to the total galactic column density. Column (12): suggested classification of the optical candidate counterpart from the *WFI* catalogue. MS indicates a main sequence star, QSO indicates a quasar, WD indicates a white dwarf, Sbc and vB2 indicate a spiral galaxy and a blue compact galaxy respectively. Column (13): proposed source classification of X-ray source with warning flags: ^a the source classification is likely but not secured by the identification of its optical counterpart; the candidate optical counterpart is unclassified, or poorly classified, or undetected; ^b the source classification is uncertain because the best-fit N_{H} value is too low for AGNs and too high for stars; ^c the X-ray spectrum is not in agreement either with the magnitude or with the colour-based classification of the candidate optical counterparts; ^d the source X-ray spectrum is not unambiguously determined, and/or the spectral parameters have large errors.

For 18 X-ray sources the proposed classifications reported in Table 5 (11 AGNs and 7 stars) are uncertain because of inconsistencies between the classification indexes. For instance, we classified source #158 (XMMU J121018.4–521911) as a star since its X-ray light curve features long and short flares (see Sect. 4.2) and its candidate optical counterpart is an M3 star. However, because of its somewhat large best-fit N_{H} , we prudently flagged its classification as *b*. Instead, source #198 (XMMU J120841.6–522026) was classified as an AGN because of its *power-law* spectrum, but it has a quite low N_{H} and we flagged its classification as *b*. We classified sources #410 (XMMU J120921.0–522700) and #688 (XMMU J120959.0–523618) as AGNs but we flagged these classifications as *a* since their candidate optical counterparts are unclassified. The former was also flagged as *d* since its X-ray spectrum is not unambiguously determined.

For the 6 X-ray sources for which no fit to the X-ray spectrum was possible with the tested single model component, or different model fits yield comparable χ^2 (flagged with “*uncl*” in Table 5) we could only suggest, at most, tentative classifications. For instance, source #263 (XMMU J120928.2–522225) might be classified as a galaxy since the colours of its nearest optical candidate counterpart are consistent with an elliptical galaxy. Similarly, source #121 (XMMU J120901.3–521741) has a candidate QSO optical counterpart and might be thus classified as an AGN. For source #386 (XMMU J121043.1–522638) not even the optical candidate counterpart is classified. Source #357 (XMMU J121113.8–522532) has no candidate counterpart in our optical/NIR catalogue⁷. Source #426 (XMMU J121000.0–522747) remains unclassified, due to conflicting power-law spectral model and stellar X-ray/optical flux ratio (although within its error-circle a clear galaxy can be seen in the *WFI* images).

Based on the previous analysis, we can summarize the classification of the 39 brightest sources as follows:

- 15 sources are classified: 5 of them were already classified in Paper I, while 1 had an uncertain classification and 3 were unclassified; the remaining 6 sources are new detections;
- 18 sources have an uncertain classification: 2 of them were classified in Paper I, while 5 were uncertain and 6 unclassified; the remaining 5 sources are new detections;
- 6 source are unclassified: 1 of them was unclassified also in Paper I, while the remaining 5 sources are new detections.

Our classification analysis improves and supersedes that carried out in Paper I where, apart from the Seyfert-2 galaxy ESO 217-G29, a classification was proposed only for 7 of the remaining 23 brightest X-ray sources (30%). For these 7 sources we have now revised the classification proposed in Paper I, which is now confirmed for only 5 of them, while it is downgraded as uncertain for the other 2. Among the 6 sources with an uncertain classification in Paper I, one is now firmly classified, while the classification of the other 5 remains uncertain. Finally, 3 of the 10 unclassified sources in Paper I are now classified, while the classification of other 6 is uncertain, and only one still remains unclassified.

We note that the use of the X-ray-to-optical flux ratio, defined in La Palombara et al. (2006), as a classification evidence

⁷ We note that this source falls in a region polluted by the halo of the bright star ρ Cen, which was masked before the source extraction (see Sect. 5.3), so that no match was produced by the *X*-correlation (see Sect. 6.3). Although a star is indeed detected in the *WFI* images, close the X-ray source position, it is saturated in almost all bands so that not even crude optical flux estimates can be obtained.

is reliable. For instance, 6 of the 7 sources classified as stars have $\log(\frac{f_{\text{X}}}{f_{\text{opt}}}) < -1.5$, while 6 of the proposed AGNs have $\log(\frac{f_{\text{X}}}{f_{\text{opt}}}) > +1$. These values are indeed in agreement with the classifications proposed for X-ray sources detected in the *XMM-Newton Serendipitous Survey* (Barcons et al. 2007), where most of the identified sources have $-1 < \log(\frac{f_{\text{X}}}{f_{\text{opt}}}) < 1$, and stars and extragalactic sources have the lowest and highest values, respectively.

7.3. Faintest X-ray sources

We also evaluated the classification of the 104 remaining, fainter X-ray sources in our serendipitous catalogue. Since for all of them the lower number of counts (≤ 500) does not allow us to perform an accurate spectral analysis, the characterisation of the X-ray spectrum only relies on the source *HR*. As in the case of the bright sources (Sect. 7.2), the proposed X-ray source classifications is based on the source *HR* and on the X-ray-to-optical flux ratio $\frac{f_{\text{X}}}{f_{\text{opt}}}$, using the classification scheme devised in La Palombara et al. (2006). When a reliable classification of the optical/NIR candidate counterparts was found, we also used this information as a further classification evidence. Based on the *HR* distribution, we assumed that sources with an *HR* < -0.9 have spectra corresponding to coronal emission from normal stars, while sources with *HR* > -0.5 are either extra-galactic (normal or active galaxies or cluster of galaxies) or accreting binary systems (XRBs or CVs). Because of the typical *HR* errors, we considered sources with intermediate values ($-0.9 < \text{HR} < -0.5$) as borderline cases and thus we did not consider this parameter compelling for our source classification. For sources affected by too large errors on the *HR* this parameter was not considered at all. As in Sect. 7.1, when no candidate counterparts were found we assumed the $R = 23.97$ limiting magnitude of the *WFI* catalogue to compute the $\frac{f_{\text{X}}}{f_{\text{opt}}}$ lower limit.

Following the same decision-tree approach used to classify the brightest X-ray sources, 4 of the 25 sources with no candidate counterpart remained unclassified, while all the remaining 21 sources were identified with an AGN.

On the other hand, among the 36 sources with a single candidate counterpart 10 were identified as stars (2 sure and 8 uncertain), 19 as AGNs (8 sure and 11 uncertain) and 2 with galaxies (since the *WFI* images show an evident extended source as counterpart). The other 5 sources remained unclassified, due to unconstrained or conflicting hardness ratio and/or X-ray/optical flux ratio, but in the error-circle of two of them a clear galaxy can be seen in the *WFI* images. Finally, in the case of the 43 X-ray sources with two or more candidate counterparts we proposed 11 classifications as stars (10 sure and only 1 uncertain) and 28 classifications as AGNs (27 sure and only 1 uncertain), while for the other 4 sources we were unable to suggest any classification.

To summarize, we classified 21 sources (corresponding to 20% of the total) as stars and 68 sources (65%) as AGNs, while other 2 sources (2%) were identified with galaxies and the remaining 13 sources (13%) remained unclassified. We note that 17 of the sources classified as stars have $\log(\frac{f_{\text{X}}}{f_{\text{opt}}}) < -1.5$. On the other hand, 16 sources classified as AGNs have a high X-ray-to-optical flux ratio $\log(\frac{f_{\text{X}}}{f_{\text{opt}}}) > +1$. As in the case of the bright sources (see Sect. 7.2), our X-ray-to-optical flux ratios yield classifications which are in agreement with those similarly

proposed for X-ray sources detected in other surveys (Barcons et al. 2007).

8. Summary and conclusions

We analysed all the *XMM-Newton* observations of the intermediate-latitude field around 1E1207.4–5209 in order to investigate the properties of the X-ray source population. We detected 144 serendipitous sources in total; 114 of them were detected in the soft energy band (0.5–2 keV), while 87 were detected in the hard energy band (2–10 keV) band, down to limiting fluxes of $\sim 10^{-15}$ erg cm $^{-2}$ s $^{-1}$ and 4×10^{-15} erg cm $^{-2}$ s $^{-1}$, respectively. The lower number of fainter sources detected with respect to that reported in Paper I (see Sect. 2.4) mainly affects the $\log N$ – $\log S$ distribution in the soft energy band, which now features a clear flattening at the low flux end (i.e. below $\sim 4 \times 10^{-15}$ erg cm $^{-2}$ s $^{-1}$). However, at higher fluxes the $\log N$ – $\log S$ distribution is perfectly consistent with that reported in Paper I and is well above those obtained at high galactic latitudes (Baldi et al. 2002). We therefore confirm the presence of a non negligible galactic population component, in addition to the extra-galactic one. In the hard energy band, the $\log N$ – $\log S$ distribution is fully consistent with that reported in Paper I and with those obtained both in the Galactic plane (Ebisawa et al. 2005) and at high Galactic latitude (Baldi et al. 2002), confirming that the distribution is dominated by extra-galactic sources. Thanks to the increased count statistics, we could perform a variability and spectral analysis of the 40 brightest sources. For 10 of them, we spotted a large flux variation between the 2002 and 2005 observations, suggesting that they are transient sources, while for other two we found evidence of variability on short timescales (~ 0.1 and ~ 10 ks). Moreover, we refined the spectral analysis of the Seyfert-2 galaxy XMMU J121029.0–522148 we discussed in Paper I, finding a best-fit redshift value $z = 0.042$, higher than the value of 0.032 reported in the literature. We also carried out a complete multi-band (*UBVRI*) optical coverage of the field with the *WFI* of the ESO/MPG 2.2 m telescope to search for candidate optical counterparts to the X-ray sources and we found at least a candidate counterpart brighter than $V \sim 24.5$ for 112 of them. By cross-identification with sources in the *2MASS* catalogue, we also provided a colour-based classification for most of them. We thus identified 27 of the brightest sources as AGNs and 7 as stars, while we identified 21 of the faintest sources as stars

and 70 sources as AGNs or galaxies. Future follow-up works will be aimed at confirming the proposed classification of the brightest X-ray sources through multi-object spectroscopy of the candidate counterparts. For the proposed AGNs we also plan to perform radio observations to achieve a better classification.

Acknowledgements. This work is based on observations obtained with *XMM-Newton*, an ESA science mission with instruments and contributions directly funded by ESA Member States and NASA. The *XMM-Newton* data analysis is supported by the Italian Space Agency (ASI). This publication makes use of data products from the Two Micron All Sky Survey, which is a joint project of the University of Massachusetts and the Infrared Processing and Analysis Center/California Institute of Technology, funded by the National Aeronautics and Space Administration and the National Science Foundation. R.P.M. acknowledges STFC for support through a Rolling Grant and INAF – IASF Milano for hospitality.

References

- Antonucci, R. 1993, *ARA&A*, 31, 473
 Baldi, A., Molendi, S., Comastri, A., et al. 2002, *ApJ*, 564, 190
 Barcons, X., Carrera, F. J., Ceballos, M. T., et al. 2007, *A&A*, 476, 1191
 Bertin, E., & Arnouts, S. 1996, *A&AS*, 117, 393
 Bignami, G. F., Caraveo, P. A., Luca, A. D., & Mereghetti, S. 2003, *Nature*, 423, 725
 Carrera, F. J., Ebrero, J., Mateos, S., et al. 2007, *A&A*, 469, 27
 De Luca, A., Mereghetti, S., Caraveo, P. A., et al. 2004, *A&A*, 418, 625
 Ebisawa, K., Tsujimoto, M., Paizis, A., et al. 2005, *ApJ*, 635, 214
 Erben, T., Schirmer, M., Dietrich, J. P., et al. 2005, *Astron. Nachr.*, 326, 432
 Groenewegen, M. A. T., Girardi, L., Hatziminaoglou, E., et al. 2002, *A&A*, 392, 741
 Hatziminaoglou, E., Groenewegen, M. A. T., da Costa, L., et al. 2002a, *VizieR Online Data Catalog*, 338, 40081
 Hatziminaoglou, E., Groenewegen, M. A. T., da Costa, L., et al. 2002b, *A&A*, 384, 81
 La Palombara, N., Mignani, R. P., Hatziminaoglou, E., et al. 2006, *A&A*, 458, 245
 Lasker, B. M., Lattanzi, M. G., McLean, B. J., et al. 2008, *AJ*, 136, 735
 Mateos, S., Warwick, R. S., Carrera, F. J., et al. 2008 [[arXiv:0809.1939](https://arxiv.org/abs/0809.1939)]
 Mereghetti, S., De Luca, A., Caraveo, P. A., et al. 2002, *ApJ*, 581, 1280
 Monet, D. G., Levine, S. E., Canzian, B., et al. 2003, *AJ*, 125, 984
 Mushotzky, R. F., Done, C., & Pounds, K. A. 1993, *ARA&A*, 31, 717
 Novara, G., La Palombara, N., Carangelo, N., et al. 2006, *A&A*, 448, 93
 Severgnini, P., Della Ceca, R., Braito, V., et al. 2005, *A&A*, 431, 87
 Strüder, L., Briel, U., Dennerl, K., et al. 2001, *A&A*, 365, L18
 Turner, M. J. L., Abbey, A., Arnaud, M., et al. 2001, *A&A*, 365, L27
 Visvanathan, N., & van den Bergh, S. 1992, *AJ*, 103, 1057
 Watson, M. G., Schröder, A. C., Fyfe, D., et al. 2008 [[arXiv:0807.1067](https://arxiv.org/abs/0807.1067)]
 Woods, P. M., Zavlin, V. E., & Pavlov, G. G. 2007, *Ap&SS*, 308, 239
 Watson, M. G., Schröder, A. C., Fyfe, D., et al. 2009, *A&A*, 493, 339